View metadata, citation and similar papers at core.ac.uk
brought to you by CORE
provided by Illinois Digital Environment for Access to Learning and Scholarship Repository

COMBUSTION SIGNATURES OF VARIOUS ENERGETIC METAL POWDERS IN A SHOCK TUBE EXPERIMENT

BY

DAVID M. JOYCE

THESIS

Submitted in partial fulfillment of the requirements
for the degree of Master of Science in Mechanical Engineering
in the Graduate College of the
University of Illinois at Urbana-Champaign, 2011

Urbana, Illinois

Adviser:

Professor Nick Glumac

Abstract

Metal additives are used in explosives and solid propellants in order to increase the energetic output and effectiveness of the explosives or fuel. Aluminum has been the primary solid fuel additive to solid fuel to improve the combustive properties of propellants. Several other metals are being considered for explosive material applications, such as reactive materials, reactive fragments, and metalized explosions. It is important to understand the burning characteristics of these materials in order to optimize their use. This study focuses on comparing the spectroscopic outputs of several energetic metals with that of aluminum. Spectroscopic analysis helps develop optical diagnostics for systems involving combustions of advanced metals. A shock tube experimental setup was used to ignite the powders, and resultant spectra were recorded. Metals tested include aluminum, boron, magnesium, hafnium, zirconium, titanium, manganese, silicon, strontium, and scandium. Finally, the resultant spectrum of each metal tested is explained, and an analysis on the results was performed.

Acknowledgements

I would first of all like to thank my adviser, Professor Nick Glumac, for his knowledge and aid in completing this project. I also would like to thank Professor Krier for not only his knowledge on the subject, but also his insights on life in general. The funding for this project this project was provided by internal funds from Professor Nick Glumac and Professor Herman Krier. I would like to thank Patrick Lynch for his help in getting the shock tube running and his knowledge of any problems I encountered. I also would like to recognize the members of my research group for their ideas and help fixing various problems, namely Brad Horn for his physical labor help and David Chonowski for his soldering skills. I would like to thank all my friends, both here on campus and back at home, for keeping me motivated and entertained while writing this thesis. Last but not least I would like to thank my family for all their emotional and financial support.

Table of Contents

List of Figures

Figure Page

List of Tables

1. Introduction

The main goal of this project was to analyze the combustion signatures of various metal powders in air using a shock tube. Metal additives are used in explosives and solid propellants in order to increase the energetic output and effectiveness of the explosives or fuel. Aluminum has been the primary solid fuel additive to solid fuel to improve the energetic properties of propellants. Several other metals are being considered for explosive material applications, such as reactive materials, reactive fragments, and metalized explosions. It is important to understand the burning characteristics of these materials in order to optimize their use. Optical combustion signatures can reveal what type of burning occurs and also what species are present during and after combustion. Knowing how a metal burns can help predict how a metal will react and perform in the desired explosive materials applications. This study focuses on comparing the spectroscopic outputs of several energetic metals with that of aluminum. Spectroscopic analysis helps develop optical diagnostics for systems involving combustions of advanced metals. This study aims to provide the base knowledge of many metals in order to stimulate further study.

Before the primary goal of acquiring the combustion signatures can be achieved, the shock tube in 1304/1308 MEL had to be fixed and optimized. At the start of this project the shock tube itself was not fully functional and could not maintain constant pressure throughout the duration of preparation. Preliminary work included leak testing the setup, determining the necessity of the metal powder injector, and general calibration of the optics setup to ensure a clear, vivid signal with every test. Once several key parts were replaced and an optics setup was determined, the primary goal of recording spectroscopic outputs was completed.

1.1 Physics of a Shock Wave

Before understanding the functionality of a shock tube, one must first understand the physics behind the creation of a shock wave and its resultant properties. Shock waves are strong pressure waves that are created by gases moving at a high velocity through a medium. The Mach number is a number that compares the speed of a gas to the speed of sound through the same medium, and is given by the equation [1]

$$M = \frac{v}{a} \tag{1.1}$$

where ν is velocity and a is the speed of sound, defined by [1]

$$a = \sqrt{\gamma RT} \tag{1.2}$$

where γ is the ratio of specific heats, R is the gas constant, and T is the absolute temperature. If the Mach number is greater than one, then a shock wave may occur.

A normal shock wave is an extremely thin region across which a flow goes from supersonic (M>1) at a low pressure to a subsonic (M<1) flow with higher pressures. This region is only a few mean free paths thick [1]. In this type of analysis, the shock is assumed to be infinitesimally small region where a jump in pressure, velocity, and temperature occurs. In the case of a shock tube, the flow is assumed to be in one direction, and there will be no changes in flow properties (temperature, density, etc.) in any direction normal to the flow. Although this is considered a jump region, conservation equations must still be followed. The three quantities conserved are mass, momentum, and energy. In a one-dimensional flow across a stationary shock wave these quantities are defined by the equations [1],

$$\dot{m} = \rho_1 v_1 A = \rho_2 v_2 A \tag{1.3}$$

$$p_1 A - p_2 A = \dot{m}(v_2 - v_1) \tag{1.4}$$

$$\frac{v_1^2}{2} + c_p T_1 = \frac{v_2^2}{2} + c_p T_2 = CONSTANT \tag{1.5}$$

where $\dot{m}$ is mass, ρ is density, A is cross sectional area, T is temperature, and c_p, is specific heat.

The subscript 1 refers to a state before the shock and the subscript 2 denotes a state after the shock has passed. The above equations only hold true if the flow is adiabatic and one dimensional, and there are no forces other than pressure acting upon the wave.

In the case of a shock tube, the normal shock itself is travelling through the tube in an approximately one-dimensional path. This approximation allows the equations to be simplified to depend only on the ratio of specific heats, γ, as well as the velocity of the shock wave, or U_s, which can be correlated to the mach number of the shock, M_s, using equation 1.1. The full derivation can be found in the Oosthuizen text, but the end result of the calculations is a series of relations that compare the pressure and temperature gradients across a normal shock. These equations are as follows [1],

$$\frac{p_2}{p_1} = \frac{2\gamma M_s^2 - (\gamma - 1)}{(\gamma + 1)} \tag{1.6}$$

$$\frac{T_2}{T_1} = \left(\frac{a_2}{a_1}\right)^2 = \frac{[2 + (\gamma - 1)M_s^2][2\gamma M_s^2 - (\gamma - 1)]}{(\gamma + 1)^2 M_s^2} \tag{1.7}$$

The assumptions for these equations are the same as before: adiabatic conditions, one dimensional flow, and the only external force acting on the fluid is pressure. In these equations, γ is also assumed to be constant, however, which does hold true in this experiment.

The importance of these equations lies in the information they tell us about all shock waves. Since the Mach number must be greater than one and the specific heat ratio must also be greater than one, these equations show the temperature behind a shock wave is significantly higher than the temperature in front of a shock wave. Likewise, although less relevant in this particular shock tube application, the pressure is also considerably higher behind the shock wave. Although these equations require several assumptions, their general principles still hold true.

1.2 Shock Tube Fundamentals

Shock tubes can be used for the ignition of metal powders and can produce extremely high temperature regions [2]. A basic shock tube apparatus utilizes the physical properties of a strong pressure wave, or a shock wave. Shock tubes create very large shock velocities that vary over a wide range. The most important characteristic of a shock wave used in shock tube experimentation is the large temperature gradient that arises, causing extremely high temperatures behind the shock wave, igniting the metal powders.

The bursting diaphragm shock tube, shown in Figure 1.1, was initially created by Sir George Stokes in 1948 [3]. This type of shock tube utilizes large pressure gradients to create high velocity gas flow. There are three basic sections: driver, diaphragm, and driven. Separating the three sections are two diaphragms, which in this case are made of thin plastic. These diaphragms have certain strength and withstand a certain amount of pressure before bursting. The driven section generally starts at low pressures and is the location of the ignition and

burning. The metal powders are loaded here, and all chemical reactions caused by the passing shock occur in the driven section. On the opposite side of the tube is the driver section, which is filled with the desired gas composition to high pressures. The diaphragm section exists between the driver and driven section and is filled to an intermediate pressure. This ensures the diaphragms do not burst early and controls when the shock is initiated. This setup is shown in the top image of Figure 1.1.

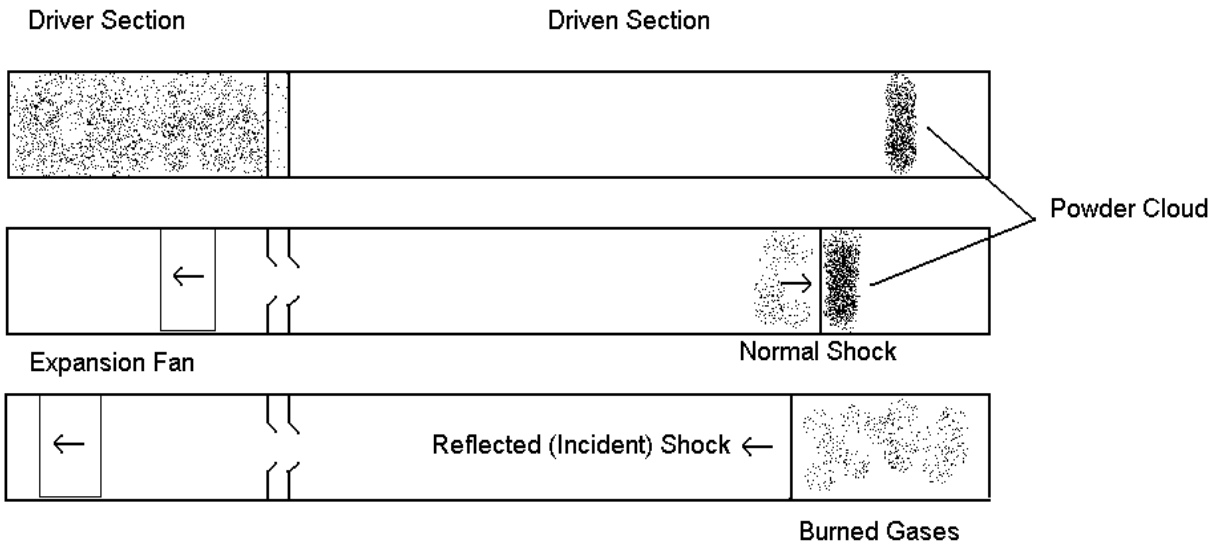

Figure 1.1: Diagram of a shock in a shock tube

Once the test is ready to run, the diaphragm section is opened to the atmosphere, which reduces the pressure significantly. This reduction causes a large pressure gradient sufficient to break through the diaphragms, and this creates gas velocities large enough to create a normal shock wave, as shown in the middle image. In addition to the normal shock an expansion fan is created travelling away from the driven section, although this does not greatly affect the combustion [4]. The normal shock travels at approximately 1500 m/s down the duration of the tube and ignites the metal powder as it passes through. Once the shock hits the endwall, a

reflected, or incident, shock occurs and travels the opposite direction down the tube. This second shock creates an even greater pressure and temperature change across the boundary layer. Through this process, temperatures up to 4000 K and pressures up to 30 atm are easily achievable in large shock tube setups [2].

1.3 Basic Combustion Information

Although the physics of combustion are quite complicated and intricate, this section aims to give a very brief overview of the important terms and aspects. Enthalpy is a thermodynamic property commonly used to energetic properties of a system. A change in enthalpy can be separated into two parts: a change in thermal energy, or "sensible" energy, and a change in bond energies. Chemical reactions break bonds between molecules and therefore change the bond energy. This change in bond energy creates a change in enthalpy known as the standard reaction enthalpy and is simply the difference between the sum of the products' enthalpies and the sum of the reactants' enthalpies [5]. In the case of combusting metals, the standard reaction enthalpy is also known as the standard enthalpy of combustion, and is always a negative quantity, which implies energy is leaving system and doing work on the surroundings. The heats of combustion of several energetic metals are shown below in Table 1.1 [7]. This table shows that hydrocarbons tend to have a higher energy output per gram of fuel. Although this may seem desirable, solid propellants also contain the oxidizer. Therefore, one must consider the amount of energy produced per kilogram of the fuel and oxidizer combined. This causes solid metals to be more desirable than hydrocarbons in several applications. The general strategy behind the selection of metal powders tested in the experiment is explained in Section 3.3.

Table 1.1: Sample Heat of Combustion Table [7]

Fuel	State	Combustion Product	Kcal/g of fuel	Kcal/g of fuel + O_2	Notes
H_2	gas	H_2O	33.9	3.79	
CH_4	gas	CO_2, H_2O	13.3	2.66	
C_2H_2	gas	CO_2, H_2O	11.9	2.93	
Be	solid	BeO	16.3	5.88 (1)	highly toxic
B	solid	B_2O_3	14.1	4.39 (3)	difficult to ignite and does not burn to full thermodynamic potential
Li	solid	Li_2O	10.25	4.77 (2)	pyrophoric - ignites at room temperature, can encapsulate
C	solid	CO_2	7.83	2.14	
Si	solid	SiO_2	7.5	3.50	
Al	solid	Al_2O_3	7.43	3.93 (4)	
Mg	solid	MgO	5.9	3.56	highly flammable

The final piece of combustion information necessary for this study is the concept of heterogeneous vs. homogeneous burning of materials. For our purposes, homogeneous burning can be considered steady state combustion of material in the vapor phase. Heterogeneous burning is more along the lines of surface combustion [8]. In order to determine which type of burning occurs, Glassman's Criterion is used. Glassman's Criterion compares the boiling points of the pure metals with the volatization temperatures of the metal oxides produced to determine how the material will combust. If the vaporization temperature of the metal is less than the volatilization temperature of the metal oxide, then the material will burn in a manner similar to a hydrocarbon droplet [9]. This type of burning involves combustion away from the droplet surface in the gas phase. If the boiling temperature of the metal is greater than the volatilization temperature of the metal oxide, however, then primarily surface combustion will occur.

1.4 Spectroscopy Overview

In order to understand the basics of spectroscopy one must first understand the basics of energy transitions, stable states, and excitation. Niels Bohr summarized the physics of photon emission into several postulates, the first of which reads: [10]

> POSTULATE 1: An atom cannot take continuous energy values as in the classical theory by, instead it is allowed to take only certain discrete energy values E_1, E_2,… characteristics of each atom. In these allowed states the atom does not emit or absorb light.

This postulate indicates that atoms can only have certain pre-determined energy values, different for each atom. This counters the notion from classical physics that particles could have any finite amount of energy. However, by establishing the existence of the first postulate, the second postulant is discovered: [10]

> POSTULATE 2: Emission or absorption of light by an atom occurs when the atom is passing from one to another of its stationary states…

This postulate indicates that a particle only gives off or receives light when it experiences a change in its state. Only upper energy states can emit light and these need to be populated by collisions, which require higher temperatures [10]. The wavelengths of the light emitted are directly related to the energy through the equation: [11]

$$E = h\nu \tag{1.8}$$

where E is energy of emitted photon, h is the Planck's constant (6.626×10^{-34} Js), and ν is the frequency. This frequency is related to the wavelength, λ, by the equation: [11]

$$\nu = \frac{c}{\lambda} \tag{1.9}$$

where c is the speed of light (2.998×10^8 m/s). Since the energy of an emitted photon is directly proportional to the wavelength, characteristics of many materials can be easily analyzed through the field of spectroscopy.

Spectroscopy can be defined as "the detection and analysis of electromagnetic radiation absorbed, emitted, or scattered by a substance," [5] and the two most common types are emission spectroscopy and absorption spectroscopy. Emission spectroscopy is relevant to this paper and involves the detection of light emitted from a molecular or atomic transition from a high energy state to a low energy state [5]. The most important tool in spectroscopic measurements is the spectrometer, whose basic design is shown below in Figure 1.2 (Note: Mirrors may be added in various places due to geometrical constraints. These mirrors generally do not affect the spectrum). The light entering a spectrometer is redirected using a dispersing element, usually a diffraction grating, which disperses the light into a spectrum. The spectrum is then registered by a camera.

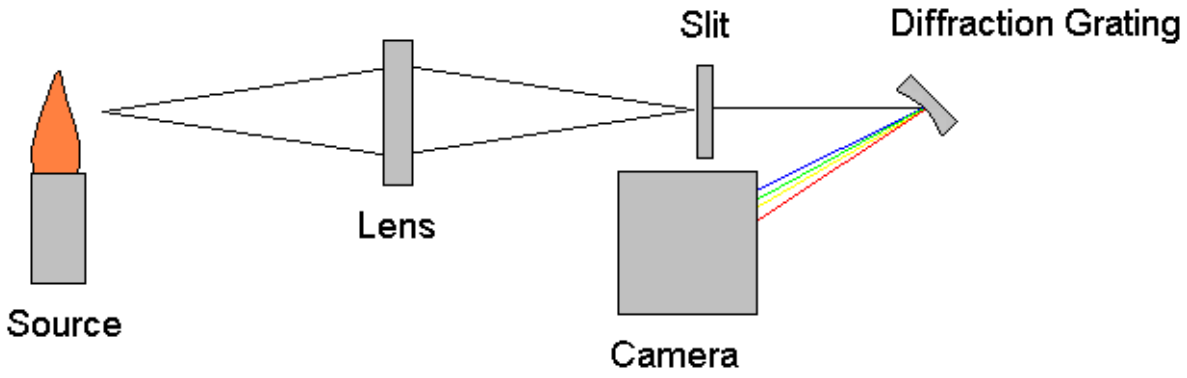

Figure 1.2: Basic Spectrometer Setup (No mirrors)

When it comes to analyzing the spectroscopic output of a material, there are several classifications that can be made. First, the spectra can be one of two types, continuous or discrete. Continuous spectra are wide bands of wavelengths that emit significant intensity, shown on the left side of Figure 1.3 [10]. Discrete spectra are narrow isolated peaks, shown on the right side of Figure 1.3 [10]. Continuous spectra tend to be a result of solids or liquids radiating whereas discrete spectra tend to be associated more with hot gases emitting from excited molecular or atomic states [10]. In this study the more prevalent spectral type is the discrete spectrum for each of the metal species.

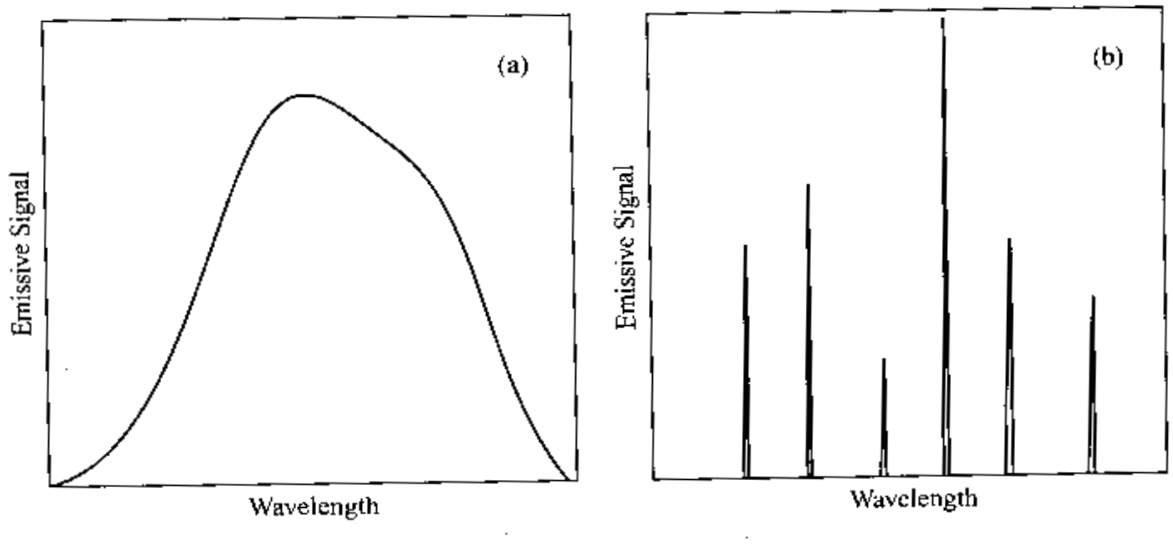

Figure 1.3: Continuous vs. Discrete Spectra [10]

When analyzing the various energy stages that are possible and their resultant spectral lines there are three different types of transitions to consider: electronic, rotational, and vibrational. A diagram illustrating the energy levels is shown below in Figure 1.4 [12]. Electronic energy level changes create the largest energy change, followed by vibrational and

rotational shifts [12]. Electronic energy deals with the location of the valence electrons around the atom or molecule. An excited atom or molecule will have electrons occupying higher energy levels. This type of energy applies to both atoms and molecules alike. Rotational and vibrational energies are not present when analyzing atoms but are important when analyzing molecules [10]. The rotational energy is relevant in molecules due to their significantly higher moment of inertia. Vibrational energy involves the compression and expansion of the bonds that hold atoms together in a molecule. Since these two types of energy change cannot be neglected, molecular spectra tend to be more complex than atomic spectra.

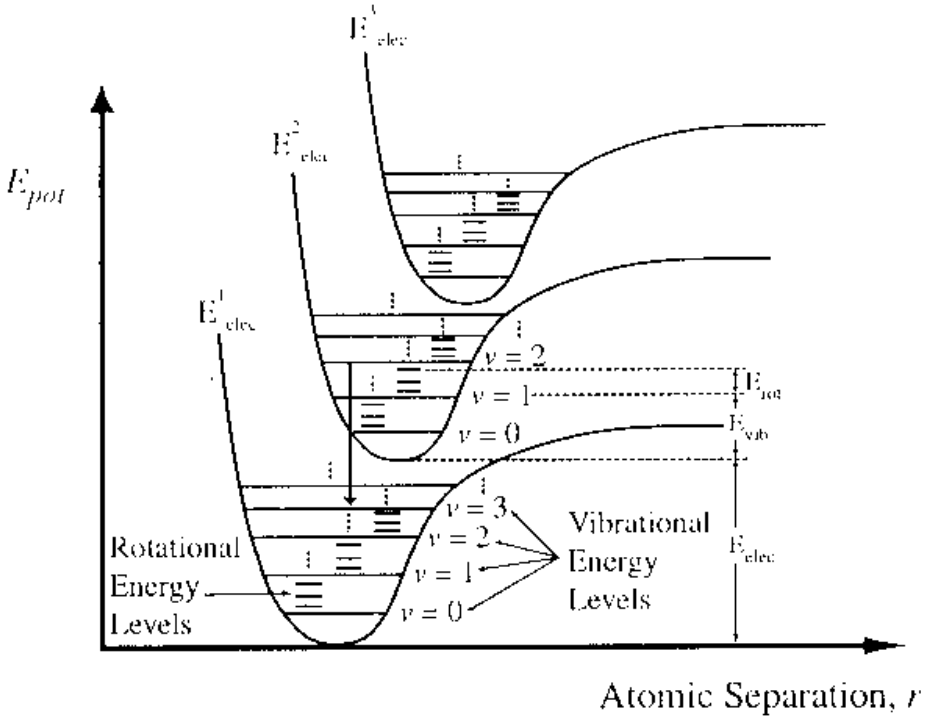

Figure 1.4: Energy Levels [12]

1.5 Solid Propellant Overview

Solid propellants have existed for several years and have been used for many purposes, from warfare to space travel. Dating back as early as second century BC, when the Chinese started using rockets, solid propellants have been used and improved [13]. The basic makeup of a solid propellant is an oxidizer bound directly to a fuel source. Once ignited, the propellant can burn rapidly and is difficult to stop, producing large amount of hot gases that can be used for thrust. Often times the fuel source is simply the rubber binder holding the entire propellant together. However, the addition of a metal powder to the mixture can greatly increase the energy output of the entire propellant. This increase is because these metals tend to have a high heat of combustion and will output a great deal of energy when burned [14].

Aluminum currently is the primary metal added to solid propellants to increase the energetic potential of a propellant, approximately making up 14-18% of the mass of a propellant [15]. Some other metal powders that are commonly added to a solid propellant are boron, magnesium, lithium, beryllium, and zirconium [13] [14]. Although boron can have a high heat of combustion and is lighter than aluminum, experiment shows an oxide coating of B_2O_3 hinders the ignition of boron particles [16]. Some of the reactant is converted to HBO_2, which is far less energetic. The presence of HBO_2 can be attributed to boron's high melting point, and as a result it is difficult to burn with high efficiency [15]. Magnesium has also been explored as a potential replacement for aluminum. Although magnesium produces significantly less energy, its byproduct ($MgCl_2$) is far less damaging to the environment than the HCl produced by combustion of aluminum. For this reason it has been suggested to replace all or some of the aluminum in solid propellants with magnesium [14]. Another option explored by researchers in the use of beryllium and it has been experimentally proven to rival aluminum in its functionality.

However, beryllium powder is toxic and creates beryllium oxide when burned, which is also toxic to humans and animals, and is therefore not safe for use in solid propellants [17]. Lithium is another metal powder with a high energy to weight ratio; however, it is pyrophoric. This means it spontaneously ignites at room temperature and is difficult to store and handle [7]. Other options that have been explored are hydride compounds, specifically aluminum hydride, boron hydrides, and beryllium hydride. These do produce high releases but also are difficult to manufacture and the quality of the material may deteriorate during storage. [15]

1.6 Reactive Materials, Reactive Frags, and Metallized Explosions

Another field in which the mechanics of metal combustion is important is the field of reactive materials. Reactive materials are a class of materials that generally combine two or more non-explosive solids which, upon ignition, react to release chemical energy in addition to kinetic energy [18]. The addition of metal powders has several positive effects on the overall blast. First, it increases the initial blast damage by increasing the rupture damage of the surface it has impacted, which increases the lethality of the explosive. Secondly, it can provide increased temperatures due to chemical reactions caused by the ignition of the metal. Third, the materials used can create reactions with critical components of the target, such as carbon shorting of electrical equipment [18].

Aluminum has been used as an additive to explosives, known as aluminized explosives, since they were initially tested in 1900 by Roth [19]. When aluminum is burned in this scenario, a small coating of Al_2O_3 forms, which causes a slower burning time. This longer burning time can achieve higher temperatures, larger blast, incendiary effects, and increased bubble energies for tests performed underwater [19]. The addition of this aluminum, and other metal powders, creates a heterogeneous mixture which provides a smaller increase in performance than a theorized homogenous primary explosive [20]. It is also theorized that the metal powders burn more slowly than the rest of the explosive and their energy release does not affect the detonation front. It is important to understand the burn characteristics of many types of metals in order to optimize reactive fragments and metalized explosions.

1.7 Previous Work and Motivation

Optical spectroscopy is a technique that as been applied to several different experiments to discover many characteristics of burning metals. It is one method of acquiring experimental data that can explain burning tendencies of metals. Aluminum is one of the most commonly tested metals, and its properties are well known. Its emission spectrum has been used to determine the burning temperature profile of not only the aluminum powder but also its aluminum monoxide combustion product [21]. This is accomplished by calculating the light intensity from the resultant spectra, which is related to the temperature through simple equations. In order to achieve the flame temperature profile of the aluminum monoxide, the AlO $\Delta v=-1$ was fitted against a theorized spectrum, which accepts five input parameters and optimized for the best fit [21]. Optical spectroscopy has also been used to learn about the burn times of aluminum particles and how they changed based on particle size [2].

Other metals have also had significant work performed on them, mainly boron and magnesium. Boron emissions in an optical bomb were studied in early research and the locations of boron monoxide (BO) and boron dioxide (BO_2) [22]. These bands spanned from 200 to 900 nm and appeared during high temperature particle combustion. Also in this experiment they measured gray body emission to be very minimal, which indicates efficient combustion of boron particles. Emission spectroscopy is also important because it helps determine what species are present during burning, which can be helpful in determining the efficiency of burning. For example, in environments high in nitrogen BN was determined to be a product, which indicates two stage burning [23]. Spectroscopy also helps determine the existence of BO, BO_2, B_2O_3, and any other products that may arise. Another use for spectroscopy during burning experiments is intensity readings. For example, in an environment high in NO, boron burns with less intensity

[23]. Using spectroscopic analysis, it can be theorized that less B_2O_3 forms because some BN is created, which is far less energetic. Another important burning quality emission spectroscopy can reveal is ignition delay. Since boron oxidation generates a layer of B_2O_3 on the outside of the boron particles, it is relevant to study the amount of time before the metal ignites fully. One method for determining this quality is through the use of emission spectroscopy to determine what products exist at any given point in the experiment [23].

The primary goal of this experimentation is to identify the combustion signatures and spectroscopic outputs of a variety of energetic metals that have not been extensively tested. Although aluminum and boron have been thoroughly tested and documented, other metals may have more desirable burning characteristics. This study aims to test a wide array of metals in a low resolution setting to collect spectroscopic signatures and data from which diagnostics can be developed. This paper will lay the groundwork for future work by collecting the spectroscopic outputs of untested metals as well as provide some insight as to which metals warrant further experimentation.

2. Experimental Equipment and Procedure

The shock tube used for this experiment is located inside 1304/1308 MEL. As shown in Figure 2.1, the setup of a shock tube is far more complex than simply three different piping sections held together by nuts and bolts. In addition to the shock tube itself, there is the control panel, which controls the gases being removed and input into the tube. There is also a metal powder injector that can be used to create a cloud of powder for the shock to pass through. In addition to all parts that contribute to the functionality of the shock tube, there is a data acquisition system that captures data and images from the shock's path and combustion of the metal powder.

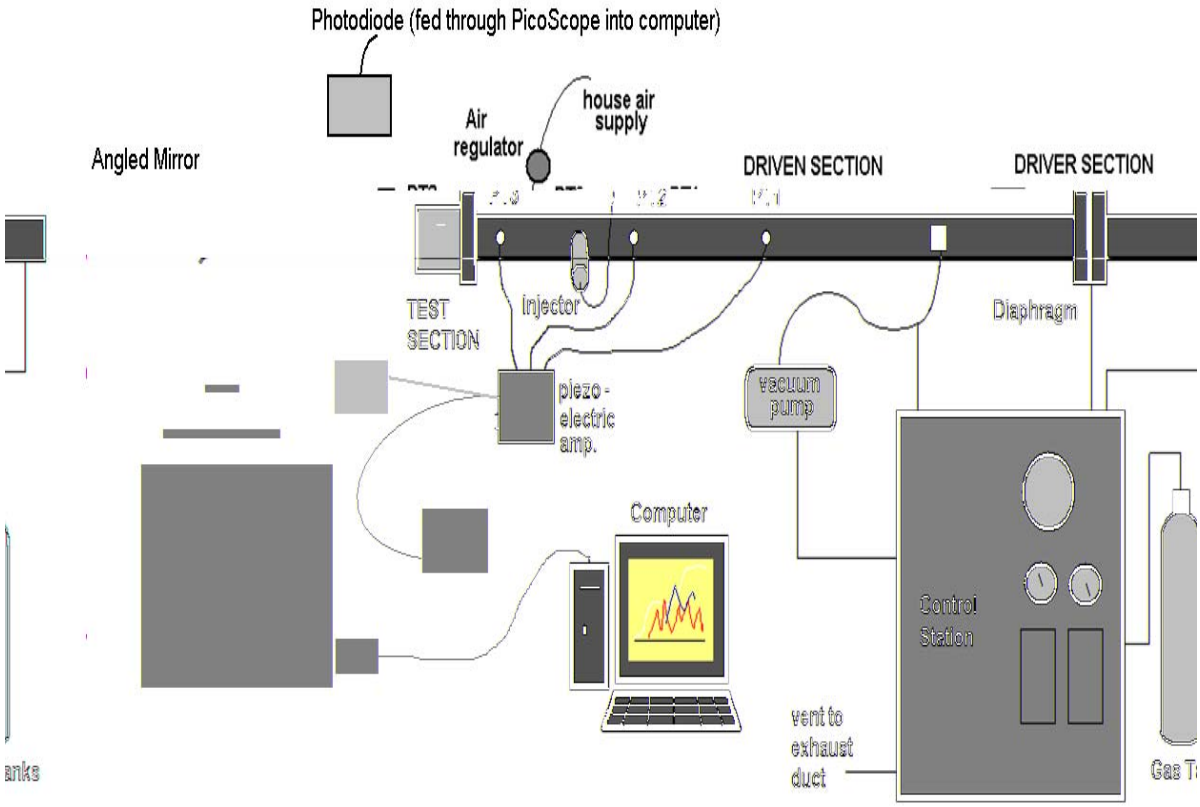

Figure 2.1: Drawn Figure of the Shock Tube Apparatus

2.1 Shock Tube

The tube itself is 36 feet long, with 6 feet of driver section and 30 feet of driven section, and has an inner diameter of two inches. The test section, located at the very end of the driven section, is made of aluminum and has two quartz viewing windows pre-installed. Connected to the test section is a redesigned endwall piece, described in section 4.1.1, that screws into the aluminum test section. The diaphragm section is located in 1308 MEL and is the intermediate between the driver and driven sections. At each interface there are two O-rings that create a dual seal in the tube. The three sections are held in place by three 1 1/2" bolts and one 1 5/16" bolt. Pictures of the shock tube apparatus are shown below in Figure 2.2 and Figure 2.3.

Figure 2.2: Driven Section in 1304 MEL

Figure 2.3: Driver/Diaphragm Section in 1308 MEL

2.2 Diaphragms

Separating the diaphragm section from the driver and driven sections are thin polymer diaphragms. This experiment used 5.5" diameter circles cut from a .010" sheet of clear polyester film (Part number 8567K94 from McMaster-Carr). Two small notches, approximately 3/16" wide, were cut into opposite edges of the circle to accommodate knobs built into the shock tube. Loading the diaphragms was done by using a folded old diaphragm to hold the new diaphragm in place while the section was closed off. This folded diaphragm was then removed with needle nosed pliers. The amount of pressure the diaphragms could withstand was tested by vacuuming out the driven section and increasing the diaphragm section pressure until the diaphragms burst. It was determined that each diaphragm could withstand approximately 225 psi before bursting. Using these data, a driver pressure of approximately 340 psi and diaphragm pressure of approximately 180 psi was selected for the test conditions.

2.3 Control Station and Gas Tanks

The control station, shown below in Figure 2.4, controls the filling of gases, triggering of injector, and firing of the shock tube. The topmost gauge measures the pressure, relative to the atmosphere, in inches of mercury of the driven section in the shock tube. At vacuum, the pressure gauge reads approximately -28.7 in Hg. Directly below that are two pressure gauges that measure the pressure of the driver section. In the bottom left corner is the power switch that controls the power of the entire unit. In the bottom right corner is the fire switch. In order to fire the tube, all valves need to be put into the "off/fire" position. Once all of the valves are closed, the fire switch is flipped, and the fire knob is rotated counter-clockwise, which decreases the diaphragm pressure to atmospheric, causing the diaphragms to rupture.

Figure 2.4: The Control Station

The controls for filling the shock tube are in the middle of the control panel and control the standard industrial gas tanks, ordered from SJ Smith. For the course of the experiments at hand, only a helium tank was connected to the control panel. In order to load gas into the tube, the gas tank knob must be first be switched to the on position, and the gas tank must be open. The control panel acts as a regulator, and thus a regulator connected directly to the tank is not necessary. Once the gas is selected, the regulator pressure is set with the large red handle. When the desired pressure is reached, the "pressurize diaphragm" knob is briefly opened. The same procedure is done with the "pressurize driver" knob to fill the driver. Once the experiment is completed, the fire knob is closed, and the "vent shock tube" knob is opened to expose the tube to atmospheric conditions. The control panel can also fill the tube with a desired composition using the various input gas lines, shown in Figure 2.5 below.

Figure 2.5: Injector Control and Gas Inlet Lines

The control panel also controls the injection of metal powders. After the tube is filled to the desired composition, the injector (if being used) can be triggered using the button of the silver box, shown above in Figure 3.5. This switch is connected to a gas tank inside the control panel and sends a burst of air through the injector, forcing the powder into the tube. The pressure of the burst can be controlled through a knob located about 2 meters from the end of the endwall.

2.4 Measurement Equipment

There were several components to the optical setup for this experiment, and their arrangement is shown below in Figure 2.6. Light emission from the test section escapes through the viewing window and is reflected off a standard mirror at a 45° angle, through a convex lens, and into a TRIAX 190 spectrometer. For tests involving longer wavelengths a piece of plexiglass was also placed in the beam's path to act as a long pass filter. Inside the spectrometer a 300 grooves/mm grating with a blaze wavelength of 405 nm was used to convert the incoming light to a spectrum, which was focused onto a GARRY 3000 camera. This camera recorded 3000 pixels of data and output its data to a program called SpectraArray. Each pixel covered approximately 0.115 nm, and the resolution achieved was 15 pixels, or 1.7 nm. The two ranges that were tested were 194-538 nm and 445-779 nm. For calibration purposes the spectrometer slit opening was 100 μm during calibration, although it was varied significantly during testing. As the shock passed through the tube, a pressure transducer located approximately 10 cm from the test section experienced a voltage increase sufficient enough to trigger a pulse generator. This pulse generator then output a pulse directly into the camera and an image of the explosion was recorded. More detail about the optical setup is given in Section 3.2.

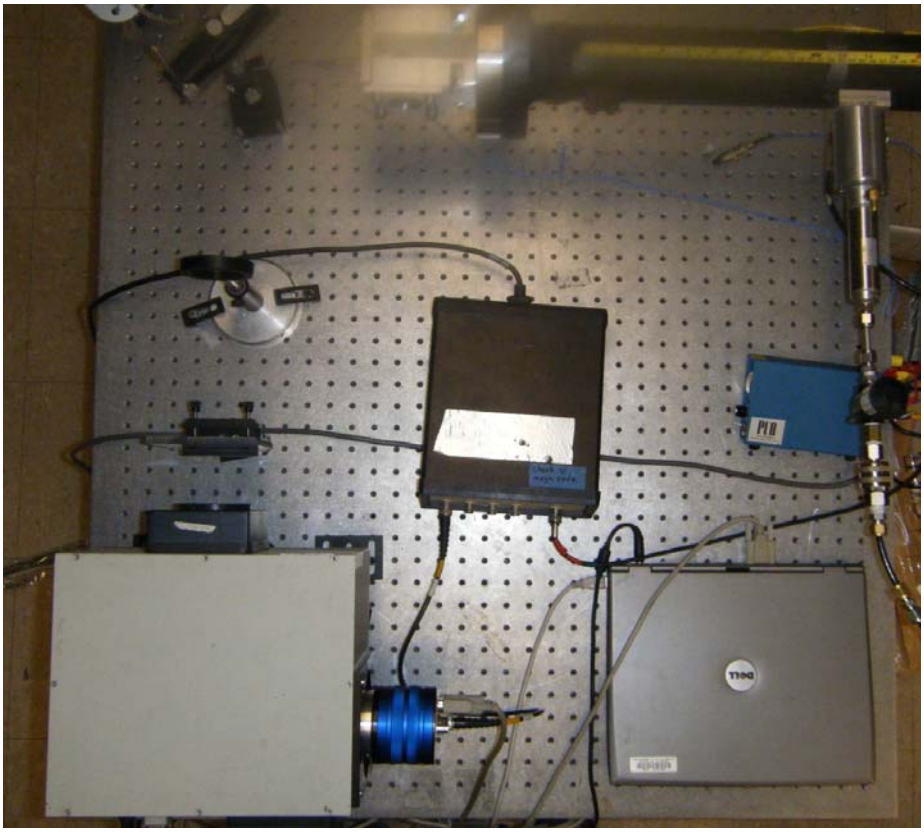

Figure 2.6: Picture of Optical Setup

In addition to the optical data collected, pressure transducers were placed at 0, 10, and 137 cm from the test region to record pressure data from the shocks. These signals were passed through a Piezotronics amplifier before passing through a PicoScope.. The settings used are shown below in Table 2.1. The PicoScope had an input characteristic of 1 MΩ with single-ended BNC connectors. These data were then outputted to the PicoScope software using a USB connection. Although these data were not directly used in the analysis of the combustion signatures, the data were quite useful in troubleshooting and ensuring consistency throughout the duration of the experiments.

Table 2.1: Settings for Transducers and Photodiode

PicoScope Slot	Input	Distance From Test Section (cm)	Amplification	PicoScope Setting
A	Photodiode	0	N/A	±5 V DC
B	Transducer PCB 134A	0	100x	±50 mV AC
C	Transducer PCB 123A35	10	10x	±20 V AC
D	Transducer PCB 132A35	54	1x	±20 V AC

2.5 Powder Injector

The powder injector, shown in Figure 2.7 and whose necessity is discussed in Section 4.4, is located approximately 35 cm from the test section of the driven section and controls the amount of powder entering the stream of the shock. The pressure burst from the trigger, mentioned above, causes a piston in the apparatus to suddenly thrust forward and expel the metal powder through a series of small holes. These holes cause the powder to disperse evenly and create a uniform cloud of particles throughout the entire shock tube.

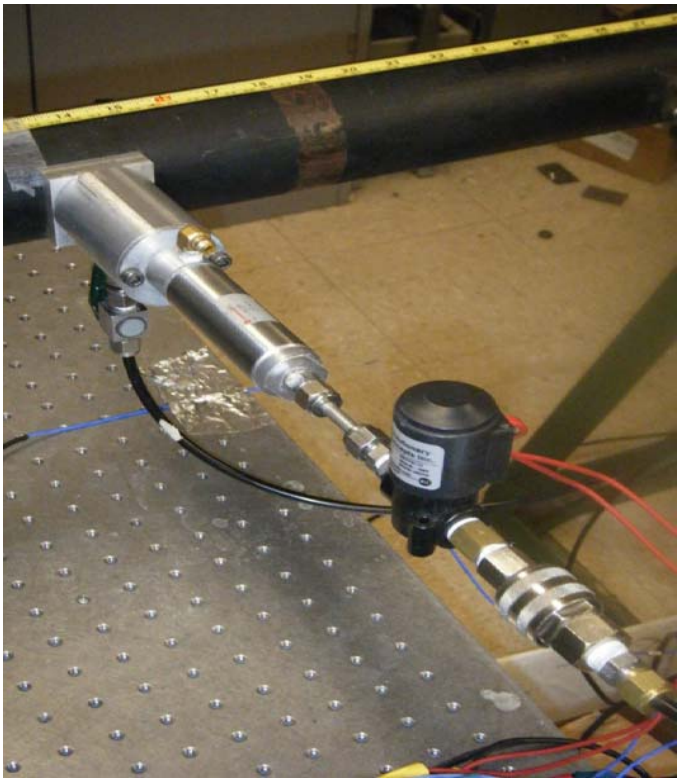

Figure 2.7: Powder Injector

2.6 Alignment LED

In order to test the alignment of the optics setup an LED light was connected to a power source and placed into the test section of the tube. While the LED was shining, the mirror and lens were adjusted to create a focused beam onto the spectrometer inlet slit. This process was completed several times throughout the course of the experiment to ensure the alignment of the optics setup was not altered between tests

3. Preliminary Work

Before any testing could be completed, the experimental setup required some maintenance, and some of the parts need to be updated. The entire shock tube was leak tested, and various sections were determined to be problematic. These sections were replaced, and the shock tube's ability to maintain pressure was increased significantly. Next, the quality of the injector was analyzed and it was determined the injector was not necessary for spectroscopic signature analysis. Next, the metal powders to be tested were selected on a basis of energetic output, economic feasibility, general availability, and potential for use in relevant applications. With the experimental setup and raw materials in hand, the optics system was selected and calibrated to create the optimal combustion signature output.

3.1 Leak Testing

The first problem encountered when attempting to use the shock tube was a significant leakage problem from the driven section of the shock tube. Several parts of the shock tube were isolated and tested for leaks and the leakage problem was found to be attributed to two locations: the endwall and the manifold connecting the gas tanks to the driven section. These two parts were redesigned and implemented into the existing shock tube setup in an effort to increase the capability to maintain vacuum.

3.1.1 Endwall Redesign

In order to create a vacuum seal, o-rings are utilized to prevent the passing of gas through the gaps between two components of an assembly. These o-rings sit in a groove in one of the parts, called a gland, and protrude slightly. In order for a proper seal, the gland design must

allow for the o-ring to compress yet still remain in contact with the other surface. In the previous endwall design the glands were either not designed correctly or not manufactured correctly and only one small o-ring was being used. The new design, shown below in Figure 3.1 and details shown in Figure B.1, utilizes two larger O-rings designed to the specifications of the Parker O-ring handbook [24]. Also incorporated into the new endwall was an increase in viewing window diameter to allow more light to escape the tube and a PCB 109A pressure transducer slot. Due to manufacturing difficulties, the endwall that was created differs slightly from the designed endwall (Figure B.1).

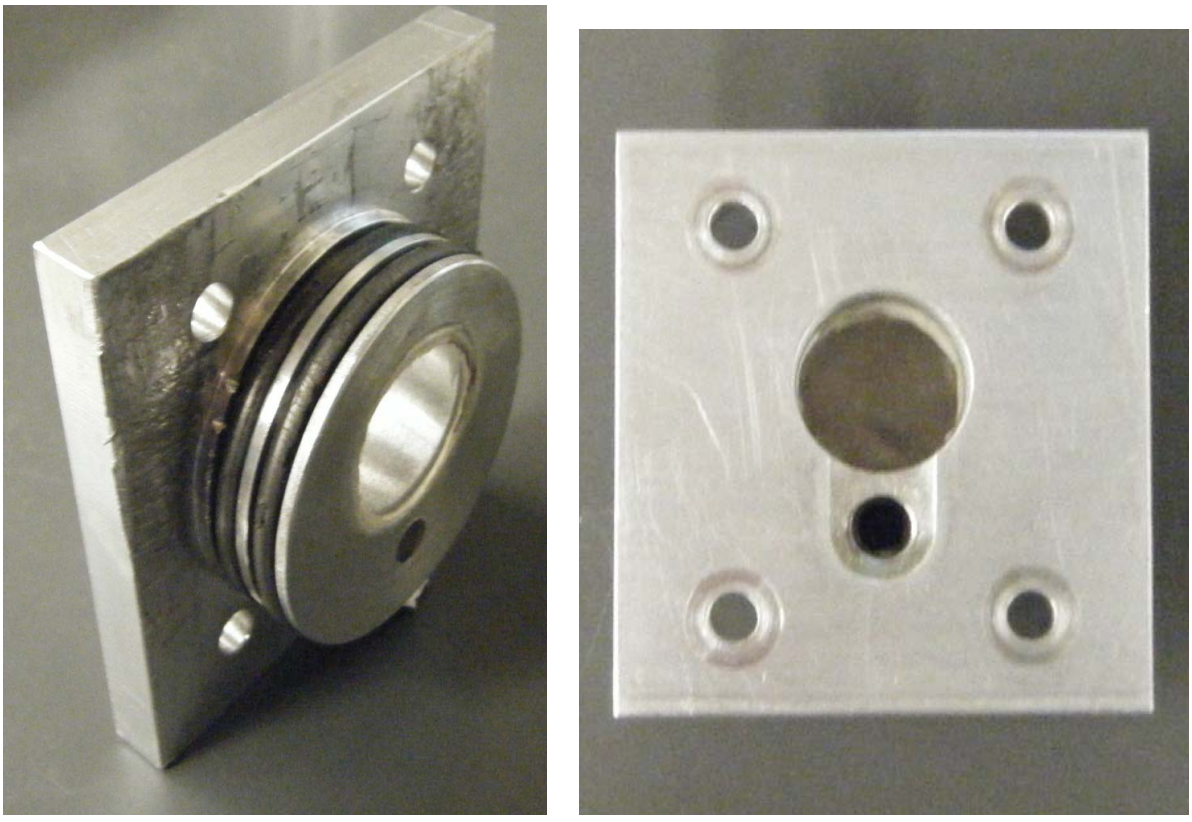

Figure 3.1: Pictures of New Endwall

3.1.2 Manifold Redesign

Another spot of potential leaking was the manifold that connected the industrial gas tanks to the driven section of the shock tube. The old design was unreliable and would allow the passing of gas if the handle was not adjusted to the perfect location. Some experimentation was done to determine if the addition of a simple O-ring would solve the problem; however, it was determined that the entire part needed to be overhauled. Several iterations of a new design were explored, although many were not physically possible to manufacture. Finally, a three piece design, shown in Figure 3.2 below, was settled upon and created. Before assembly of this design was completed, a 0.625" diameter hole was drilled into the shock tube at the same location of the existing tapered hole previously used by the old manifold.

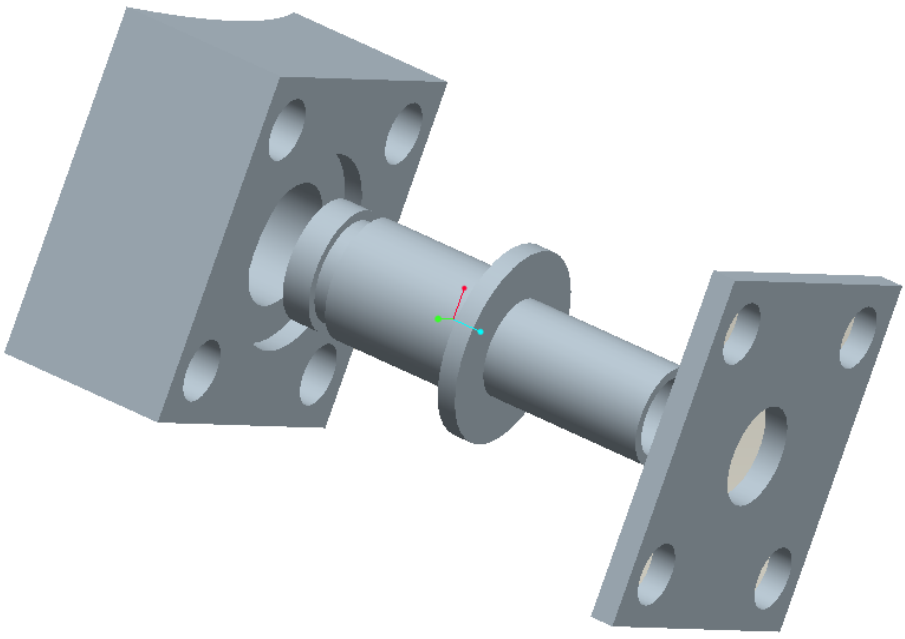

Figure 3.2: Exploded View of New Manifold

The new design consists of three simple parts held in place be ¼-20 set screws. One piece is a simple tube that on one end seals with the 0.625" hole in the shock tube, while the other side mates with a ½ inch SwageLok tubing. This SwageLok tubing then tees into the vacuum pump and the gas input lines. The second piece is a block with curved side to mate with the shock tube. The block has a hole running through the center that holds the first piece in place laterally. The third piece is a flat plate that prevents the entire setup from being pushed out of the shock tube axially. Set screws hold the three pieces together on the side of the shock tube. Detailed drawings of the new manifold are shown in Appendix C

3.1.3 Leak Test Results

The end result of all the newly designed pieces was a significant increase in the amount of time the shock tube could maintain a low pressure. The results are shown in Figure 3.3. With the old endwall and manifold attached to the tube, ambient air would immediately leak into the shock tube, and pressure would increase 36.8 torr in just 30 seconds and 102.9 torr in just over 90 seconds. Comparing this data with our starting driven pressure of 34.9 torr, it takes under thirty seconds for the driven pressure to change 100%. This pressure change was unacceptable since the driven section needed to be kept as close to vacuum as possible, and once the tube is sealed off it takes approximately 120 seconds to run a test.

The effects of an increased pressure in the driven section are quite important and cannot be ignored. A larger pressure in the driven section creates a smaller pressure gradient across the shock wave that is coming through the tube. Since the pressure gradient across the shock is smaller, the Mach number of the shock wave is also decreased. Another effect of a small pressure gradient is a small temperature gradient. The end result is a final pressure and

temperature that is lower. In order to obtain repeatable final temperatures and pressures that can be calculated for quantitative use, leakage of pressure into the driven section must be kept to a minimum, and the hardware needed to be reworked. After installing the newly designed parts and replacing the old tubing, the pressure remained constant for significantly longer. It took approximately 150 seconds to notice an appreciable difference (~10 torr) in driven section pressure. With the new parts, a change of 10% was not realized until after 120 seconds. This duration of essentially zero leakage is sufficient to successfully perform the experiment.

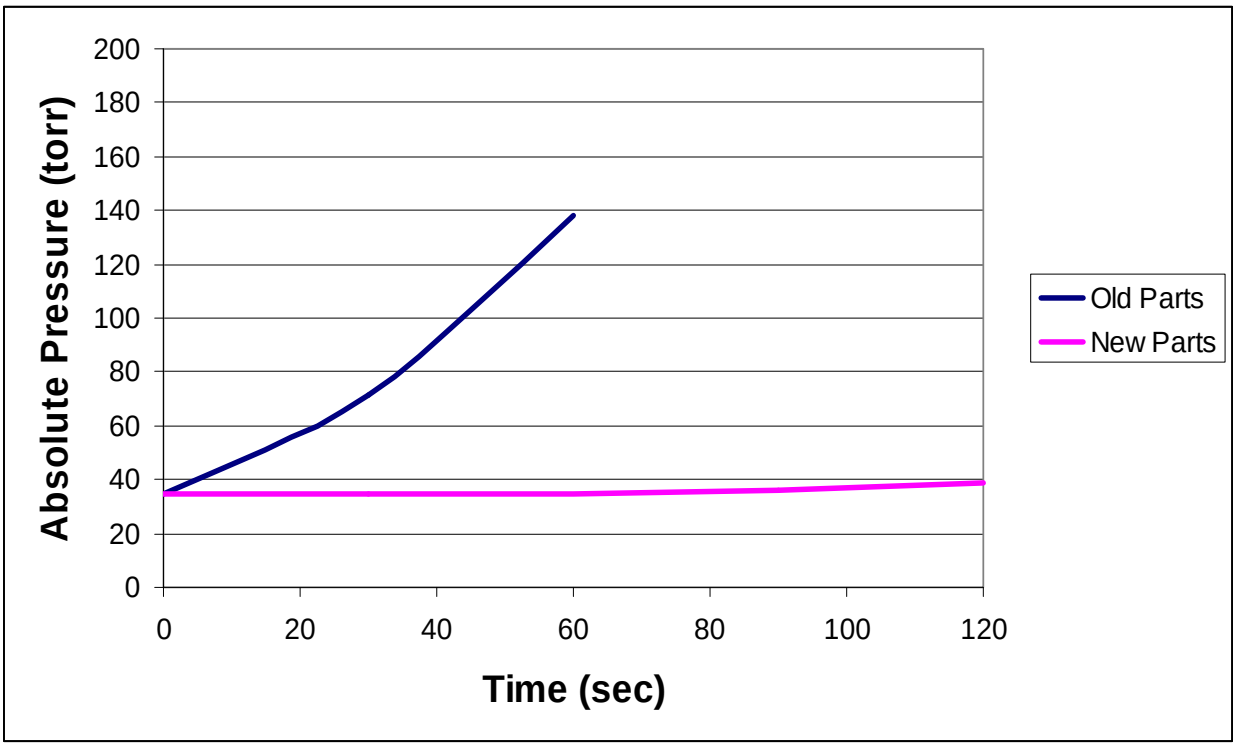

Figure 3.3: Pressure Leak Test Results

3.2 Calibration of Measurement Equipment

Before any testing could be completed, a useful data collection system that provided consistent results needed to be devised and calibrated. The optics package (described in Section 2.6) was selected because it provided a low resolution look at the spectroscopic outputs of the burning metal powders that allowed for a wide range of wavelengths to be explored. Although the goal was to acquire the entire spectrum, from wavelengths of 200-800 nm, it quickly became evident that two ranges would need to be analyzed because the measurement equipment cannot capture the entire range of wavelengths in one test. It was decided that one region would focus mainly on the ultraviolet region and would range from 200 – 450 nm, and the other region would range from 450 – 800 nm. The use of two ranges actually proved beneficial because the lower wavelengths tended to have a weaker signal than the longer wavelengths. These benefits are discussed in Chapter 4.

The first task was to determine the most consistent pressure transducer to use as a trigger for the optics setup. After appropriate amplification settings were mastered (listed in Chapter 2), a test using aluminum powder was completed, as shown below in Figure 3.4. The importance of this test was to determine which pressure transducer would be used to trigger the pulse generator. The green curve represents the transducer located 10 cm from the endwall, the red curve indicates the endwall pressure transducer, and the blue curve represents the photodiode near the endwall. This image shows a clear, near-instantaneous spike in pressure at 0 ms, which indicates the incident shock wave passing the transducer. A half millisecond later, another larger instantaneous spike in pressure occurs, which indicates the passing of the stronger reflected shock. Between these two spikes is the ignition of the metal powders, which can be seen by the rise in the photodiode voltage.

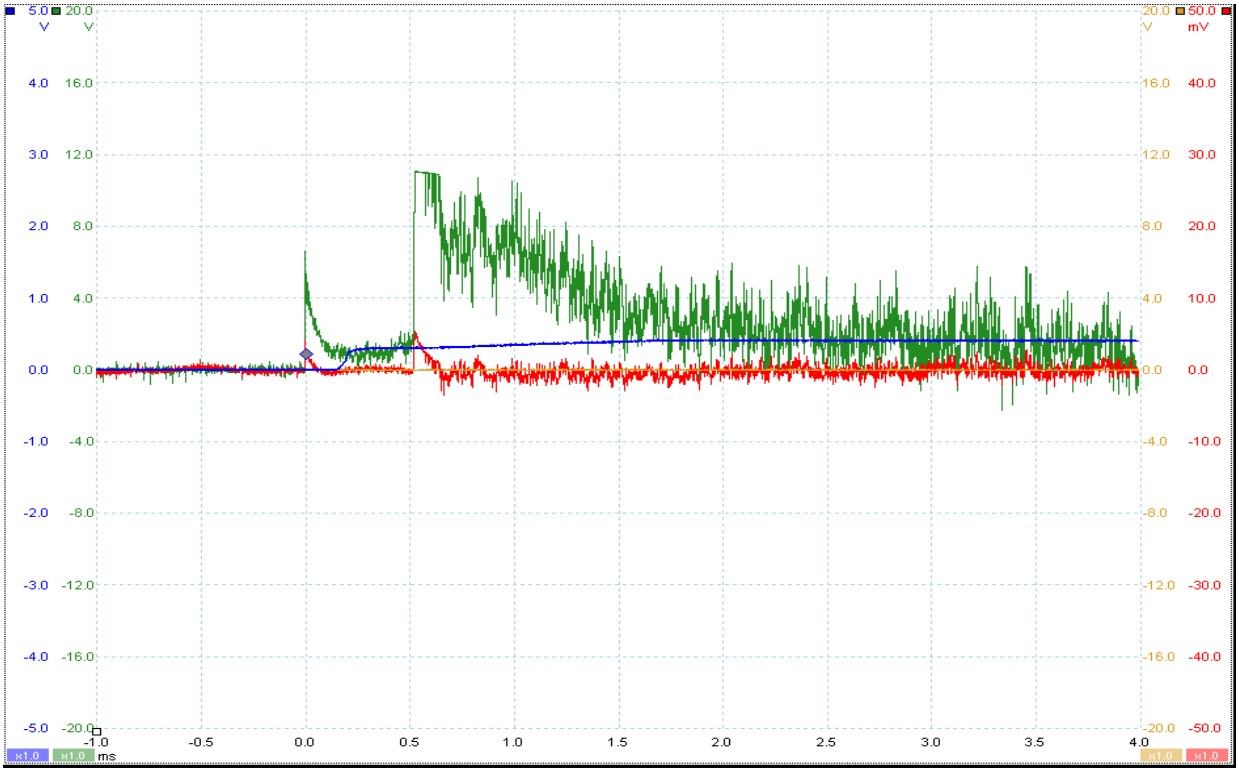

Figure 3.4: Pressure Voltages from Aluminum Test

The pressure transducer 10 cm from the endwall (green curve) was selected to be the trigger because it consistently measured between 4 and 8 volts, which was well within the threshold voltage of the pulse generator. Once the pulse generator was activated, a single pulse would trigger the detector array to capture the spectrum. These settings were repeated for every trial and continually triggered the detector array at the appropriate time to capture the combustion signal. A summary of the settings for the optical equipment is shown below in Table 3.1.

Table 3.1: Optical Details

Equipment	Details
Pulse Generator	• External gate input from pressure transducer 10 cm from test section • Triggered by 3 – 8 V • 0.9144 ms delay • Output 3.5 V, 0.5 ms pulse
Garry 3000	• Receives pulse into Ext Trig Gate • Switch settings; 1 off, 2 on, 3 on, 4 off • Internal integration equal to incoming pulse width (0.5 ms) • 1 MHz readout speed
Computer	• Spectra-Array data collection from camera (external trigger mode) • Spectrometer Control to control Triax 190

Once the triggering system was established, the detector array needed to be calibrated. The Garry 3000 outputs a data file of 3000 different intensities, one for every pixel across the opening of the camera. In order to translate these pixels to wavelengths, a mercury vapor lamp was used. The spectrum, shown in Figure 3.5, has defined peaks, which were correlated to pixel numbers in the camera and extrapolated to all pixels. This procedure had to be performed twice, once for the low region and once for the high region, as well as any time the setup was accidentally altered.

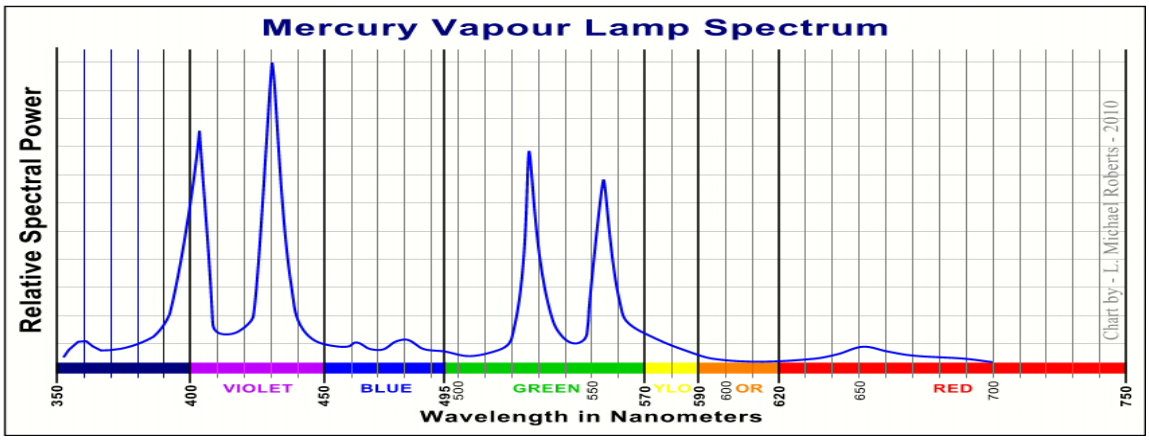

Figure 3.5: Mercury Vapor Spectrum

The final calibration for the camera involved taking a dark spectrum. This spectrum accounts for the fact that the room tests are being performed is not perfectly dark, and the detector array will always read greater than zero intensity. An image of a dark room was taken and the intensity recorded across all pixels ranged between 110 and 130 units. This file was saved, and in all subsequent tests these values were subtracted off the new data.

In most applications a light intensity calibration needs to be performed in order to obtain useful information about the intensity of light obtained during combustion. To perform this calibration an image of a known light source burning at a known temperature, such as an Oriel halogen lamp burning at 3100 K, is taken. Then a dark image of the same location is obtained and subtracted off from the image from the known light image. Future tests are calibrated to the known collected data. This calibration was not necessary and not performed for this experiment because the goal of the experiment was only to identify features of combustion, and absolute intensity was not important.

3.3 Selection of Metal Powders

When selecting the metal powders used for this test, several factors were taken into account. First, the functionally of the powder, namely the heat of combustion of the powder and the ignition temperature, was taken into account. Powders with high energetic potentials and combustions temperatures low enough to obtain in a shock tube experiment were selected. Next, a hazard analysis was performed. Metals that are unsafe to store and are dangerous in their pure state, or metals that produce toxic oxides were eliminated from the study. Third, a cost and availability analysis was performed. Metals that were too costly or not easily attainable from manufacturers were eliminated from the study. An exception to this was scandium, which was

obtained even though it was costly and slightly more dangerous than standard metals because it looked promising, and little work to date has been done on the material. In addition, metals that were readily available and used in other testing scenarios, such as hafnium, were also tested. Although the goal was to collect all -325 mesh materials, some were unable to be attained and other forms of powder were used in substitute. Table 3.2: Metal Powders Tested below lists the powders tested.

Table 3.2: Metal Powders Tested

Metal Name	Form	Size	Purity	Provider
Aluminum	**Powder**	**<75 micron**	**99%**	**Sigma Aldrich**
Boron	**Crystalline**	**-325 mesh**	**90-95%**	**Sigma Aldrich**
Hafnium	**Powder**	**-325 mesh**	**99.6%**	**Alfa Aesar**
Magnesium	**Powder**	**Unknown**	**99.5%**	**Sigma Aldrich**
Manganese	**Powder**	**-325 mesh**	**99.3#**	**Alfa Aesar**
Scandium	**Powder**	**Unknown**	**99.9%**	**Sigma Aldrich**
Silicon	**Powder**	**-325 mesh**	**99%**	**Alfa Aesar**
Strontium Chloride	**Anhydrous**	**Unknown**	**99.5%**	**Alfa Aesar**
Titanium	**Powder**	**-325 mesh**	**99.5%**	**Alfa Aesar**
Tungsten	**Powder**	**-325 mesh**	**99.9%**	**Alfa Aesar**
Zirconium	**Powder**	**<2-3 micron**	**Unknown**	**Alfa Aesar**

3.4 Injector Analysis

In most previous work performed in the current shock tube an injector was used to put the metal powder into the path of the coming shock wave. The purpose of the injector was to create a cloud of particles for uniform burning and quicker ignition. This more uniform burning aids in

quantitative calculations by knowing the timing and position history. When performing purely qualitative tests, such as recording the combustion signatures of metal powders, the injector did not prove to be necessary. Set-up time was decreased significantly by eliminating the injector.

In order to determine whether the injector was necessary to achieve quality combustion signatures, a basic test using aluminum with a slit opening of 100 micron was performed and the results are shown in Figure 3.6. The test was performed at standard operating conditions (much like those used in later tests) and was focused on the ultraviolet wavelengths. The results show essentially the same resultant curve, except the test using no injector results in a much more intense image. Although the injector creates a cloud of powder, it limits the amount of powder than can be inserted into the tube because only so much can be loaded into the apparatus. In addition, some of the metal powder never makes it out of the injector. The reduction of metal powder entering the tube results in less combustion and a weaker signal. Since quality combustion signatures could be achieved without the use of the injector, the decision was made to load powders directly into the tube. This process simply consisted of inserting a small amount of powder (~25 mg) through the hole where the injector is inserted, allowing the powder to sit on the bottom of the tube. The amount of powder per test was inexact because this was a purely qualitative study.

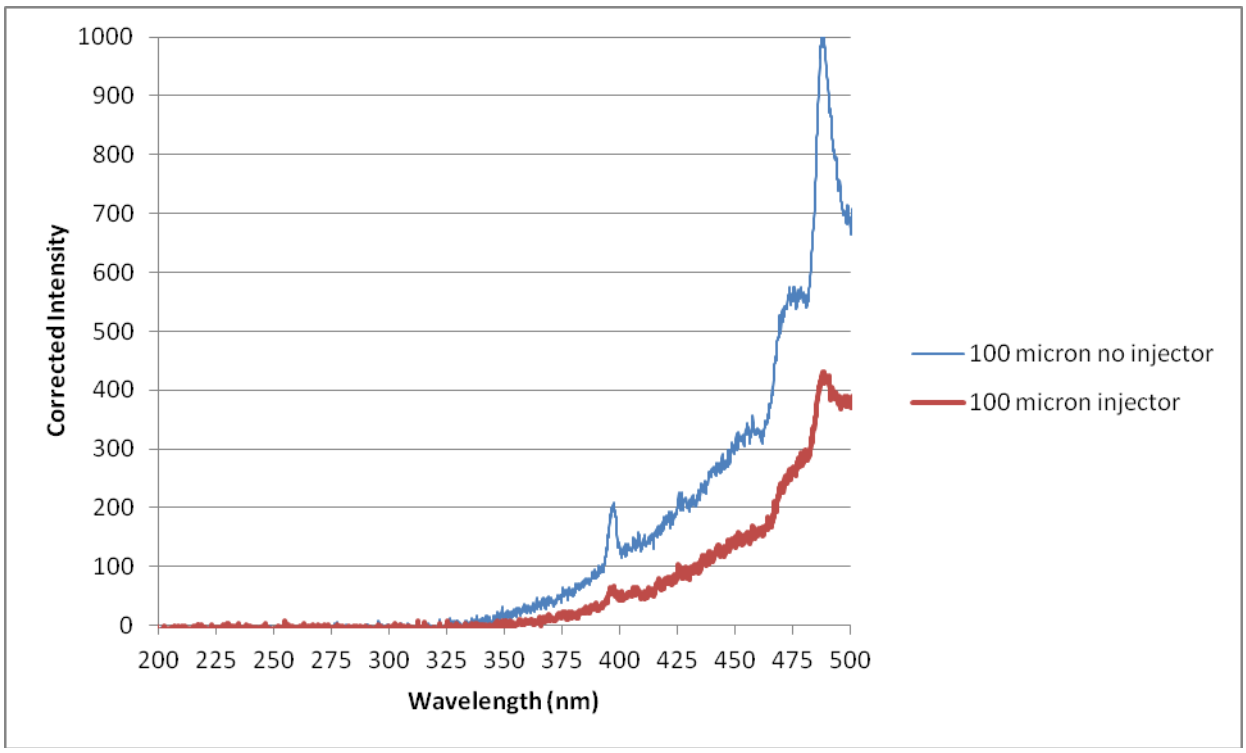

Figure 3.6: Injector Test Spectra

4. Results and Discussion

4.1 Experiment Specifications

Once all preliminary work had been completed and the shock tube was in proper working order, experimentation on the metal powders was started. The primary goal of the experiment was to collect the combustion signatures of various metal powders. For all trials the driver section was filled to ~330 psi, and the diaphragm section was filled to ~180 psi with helium gas. This setup provided a consistent shock that was easily repeatable for the duration of the testing. The measurement equipment was mainly untouched, and the settings were unaltered in an attempt to maintain consistent data acquisition for all powders. After a few trial runs, however, it became apparent that some of the metal powders burned with much greater intensity and saturated the camera more quickly. The goal was to capture the combustion signatures vividly for all metals tested, therefore the decision was made to alter the slit width opening of the spectrometer to allow the maximum amount of light in before saturating the camera. Tests to capture low wavelengths were initially tested at a 90 micron opening, and tests to capture high wavelengths were initially conducted at a slit width of 40 microns. If the resultant image was too bright, the slit width was decreased until an unsaturated spectrum was captured. For the high wavelength tests, the peak sodium doublet at 589 nm was allowed to saturate in order to make the other features of the spectrum more clearly visible.

4.2 Combustion Signatures of Metal Powders

The first tests performed were done on aluminum powder as a baseline test to compare to existing data. Aluminum was abundantly available, and there has been extensive experimentation performed on aluminum particles. Several settings were tested using the aluminum as a test subject, and eventually a base slit opening size of 90 micron was selected for

the lower wavelengths, which proved to be fairly consistent throughout the testing for all metals. For longer wavelengths, a slit size of 70 microns provided the best signal for aluminum, but this varied more greatly between the metals.

4.2.1 Aluminum

The lower wavelength results from the spectroscopic testing of aluminum are shown in Figure 4.1. As can be seen from the graph, there is only one feature of interest present, the peak at ~395 nm. This peak can be attributed to an aluminum doublet that occurs at 394.4 nm and 396.2 [10]. Due to the resolution of the experimental setup, the individual peaks cannot be resolved. There is also evidence of a possible spectral line at ~413 nm, but this may just be a result of noise and experimental error.

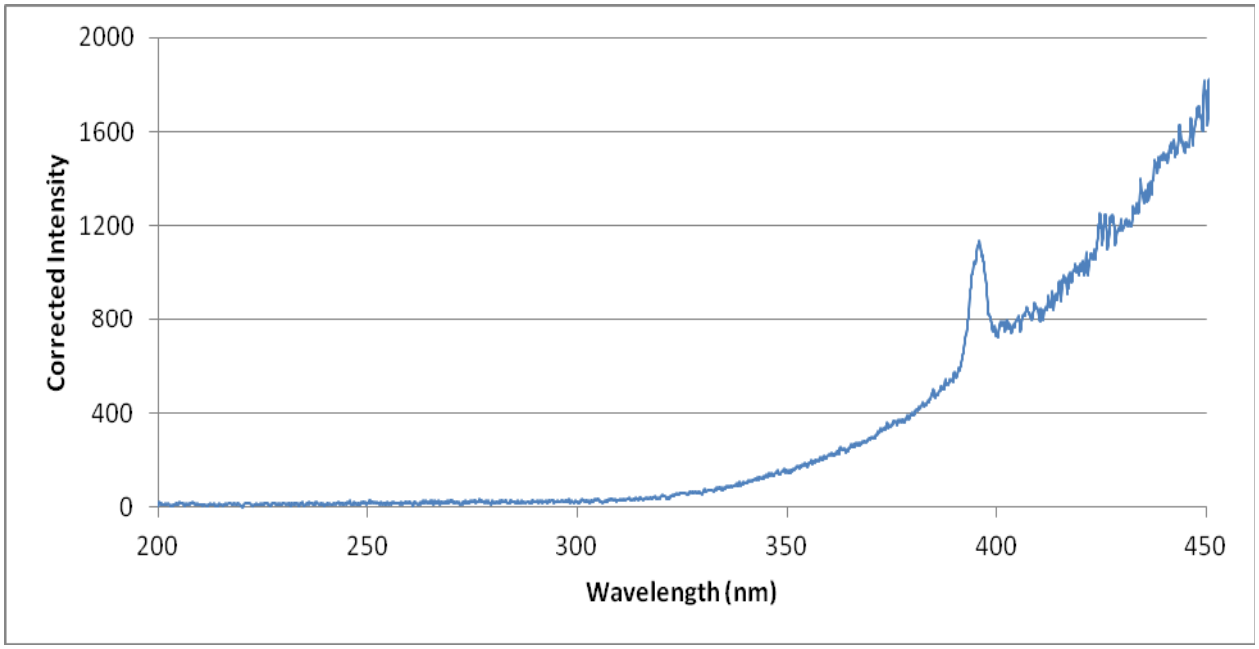

Figure 4.1: Aluminum spectrum (200 – 450 nm) with slit width 90 micron

The results from the higher wavelength region, shown in Figure 4.2, show significantly more features than the low region, which proved to be a common theme throughout all testing. The region from 450 nm to 600 nm has been tested extensively in previous experimentation. Peaks at 473, 486, 515, and 545 nm match the aluminum monoxide spectrum produced by the AlO B-X transition, as outlined in previous papers [7], as well as documented tables of

wavelengths [10]. In addition, the large peaks at 588 nm and 764 nm were identified as the sodium doublet, or the sodium D-line, and the potassium doublet, respectively. These doublets are also consistent with the literature, which indicates the validity of the wavelength calibration.

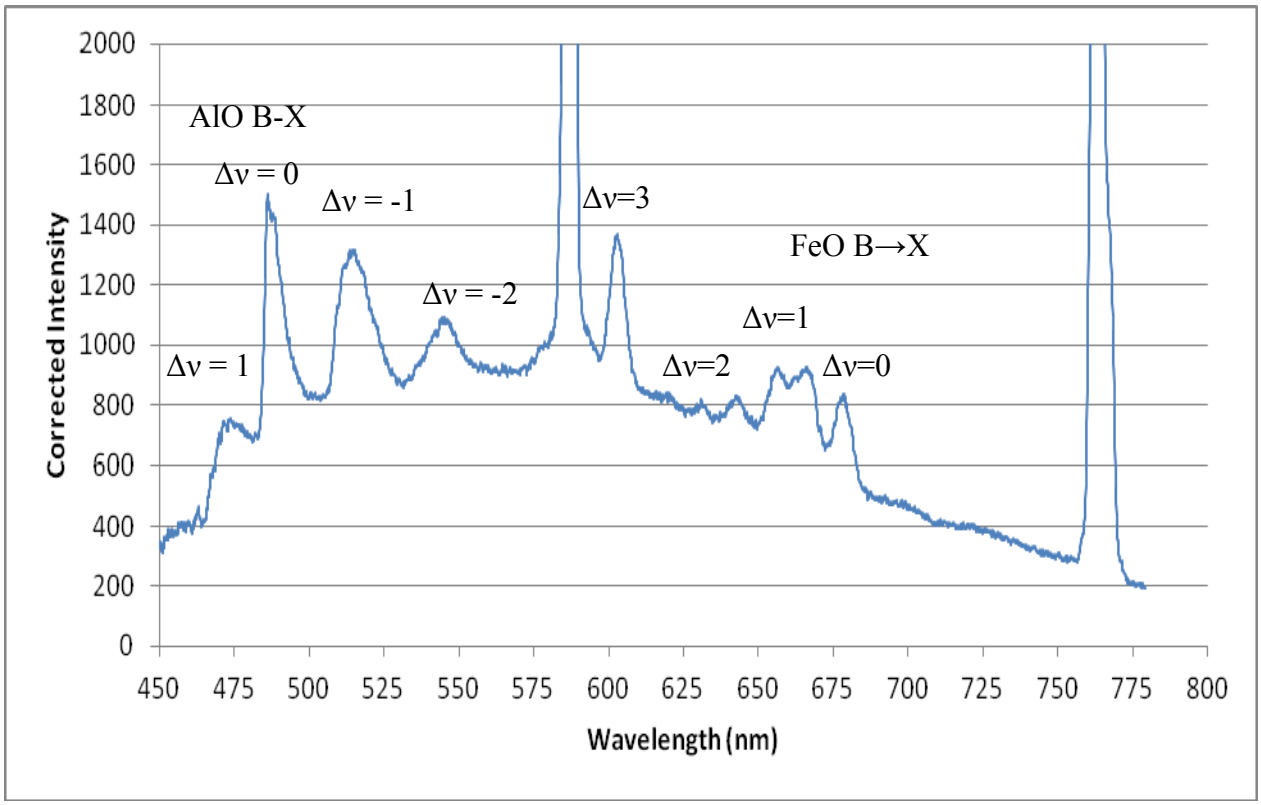

Figure 4.2: Aluminum Spectrum (450 – 800 nm) with slit width 70 micron

Aside from previously published results, interesting features appeared between 600 and 700 nm, a relatively unexplored region of aluminum spectroscopy. Previously published experiments suggest there should be no spectral lines in this region, although they appeared fairly consistently throughout the duration of the aluminum powder testing, as well as during a few other tests. Previous work in the shock tube performed by Giovanni Fiore suggest that there are iron deposits on the inside the shock tube and during experiments a small amount of Fe_2O_3 is produced. This Fe_2O_3 breaks down into FeO and produces a signal similar to the results

achieved during these tests [25]. The peaks at 603, 631, 657, and 679 nm correspond to the FeO B→X transition, and the other two peaks correlate strongly with other Fe emissions from the NIST website. This iron impurity in this system is sufficient to describe all spectroscopic images seen in the aluminum cases.

The final type of analysis performed for each metal involves Glassman's criterion. The boiling point of aluminum is approximately 2670 K [26], which is significantly lower than the vaporization point of aluminum oxide (Al_2O_3) at 4000 K [9]. Since the vaporization point of the oxide is higher than the boiling point of the metal, the metal burns likes a vapor and there are well defined molecular features in the spectroscopic output. As for the iron impurity, the boiling point of iron is again lower than the vaporization temperature of the iron, 3023 K [26] and 3400 K [9], respectively. This means the iron also burns likes a vapor, and features of gas phase combustion intermediates are also well defined in these tests.

4.2.2 Boron

Boron was an interesting case because there are several different types of boron oxide that appear during the combustion of boron. The most intense oxide that appears is BO_2 and this oxide tends to dominate the overall spectrum. BO also appears in several cases but is overshadowed by the presence of BO_2, although it can be seen at the lower wavelengths, such as seen in the 416 and 438 nm peaks in Figure 4.3. These peaks are created by the BO $A^2\Pi \rightarrow X^2\Sigma$ transition. Also shown in the lower wavelength region is the BO_2 $B^2\Sigma \rightarrow X^2\Sigma$ transition occuring at 409 nm [23]. In the higher wavelength testing region, the image is dominatinated by boron dioxide. The series of peaks ranging from 454 nm to 637 nm represents the BO_2 transition $A^2\Pi \rightarrow X^2\Pi$ [23]. It is known that the BO transitions $B^2\Sigma \rightarrow A^2\Pi$ and $A^2\Pi \rightarrow X^2\Sigma$ also occur in this region, but are overshadowed by the stronger BO_2 emission spectrum. It has also been proven that B_2O_3 is produced during the combustion of boron; however, B_2O_3 does not produce any spectral features in this region [23].

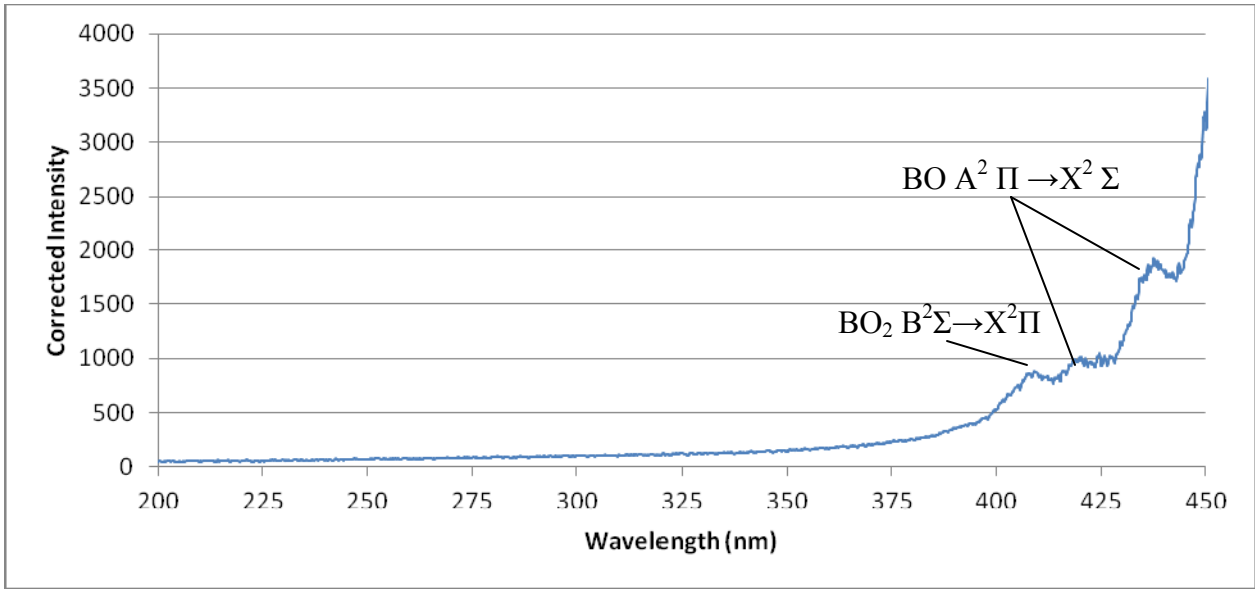

Figure 4.3: Boron spectrum (200 – 450 nm) with slit width 90 micron

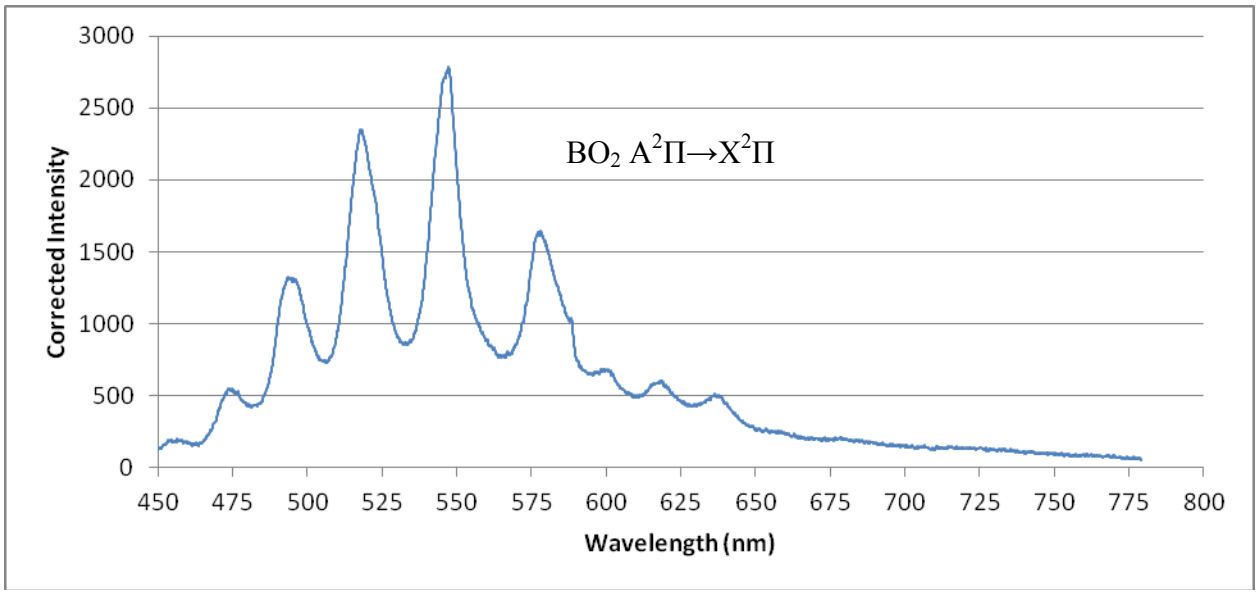

Figure 4.4: Boron spectrum (450 – 800 nm) with slit width 25 micron

Boron is an interesting metal to analyze because it undergoes two-stage burning, which can be explained using Glassman's criterion. The boiling point of boron is 3931 K, which is significantly higher than the volatilization temperature of B_2O_3, 2316 K [30]. As boron burns, a liquid layer of B_2O_3 forms on the boron particle, which prevents ignitions of the boron droplet. This indicates only surface combustion occurs during the first stage of combustion, which means this stage can be described as heterogeneous burning. Once the liquid layer of B_2O_3 has burned off, then the second stage of combustion may begin and the bare boron particle begins to combust [30]. During the second stage of combustion, homogeneous burning is observed. Since there are well defined BO and BO_2 features present in the spectra above, there must be some gas phase combustion occurring.

4.2.3 Magnesium

In the shorter region of wavelengths, magnesium showed quite a number of features that were not present in other tests, shown in Figure 4.5. It was the only material to show a number of features below 400 nm in wavelength. The series of peaks at 364, 372, 382, 291, and 402 nm correlate very closely with the MgO C→A transition centered around 372 nm. Towards the higher wavelengths, a trace of another MgO transition ending in the A state can be seen, shown in Figure 4.6. The wavelengths 591 and 619 nm resemble the start of the MgO B→A transition. This transition then becomes overshadowed by the iron impurity that was noticed during the aluminum runs. The FeO B→X transition can be seen in the peaks at 631, 655, and 679 nm in addition to the iron emission at 666 nm. The final magnesium monoxide transition that can be see in the $B^1\Sigma^+ \rightarrow X^1\Sigma^+$ transition, which is centered around 490 nm and includes the wavelengths 454, 471, 490, and 510 nm. The final peak at 510 nm is not seen due to a strong magnesium triplet produced in the area [10].

In addition to the magnesium monoxide produced, there are other peaks that appear around 518 and 548 nm. The first feature is caused by a magnesium triplet that occurs between the wavelengths of 516.7, 517.2, and 518.3 nm. Once again, this all gets convolved into one peak due to the low resolution nature of this experimental setup. The second peak, 552 nm, is a result of magnesium emission and can be seen in the magnesium spectrum [27] and is confirmed by the NIST lines holding as the Mg I emission with a relative intensity comparable to the magnesium triplet [28].

The spectroscopic output of magnesium shows several well defined features, which is usually an indicator of homogeneous burning. Upon examining the boiling temperature of

magnesium, ~1400 K [26], and the volatilization temperature of MgO, 3430 K [9], it is seen that magnesium easily fulfills Glassman's condition and the magensium droplets burn like a vapor.

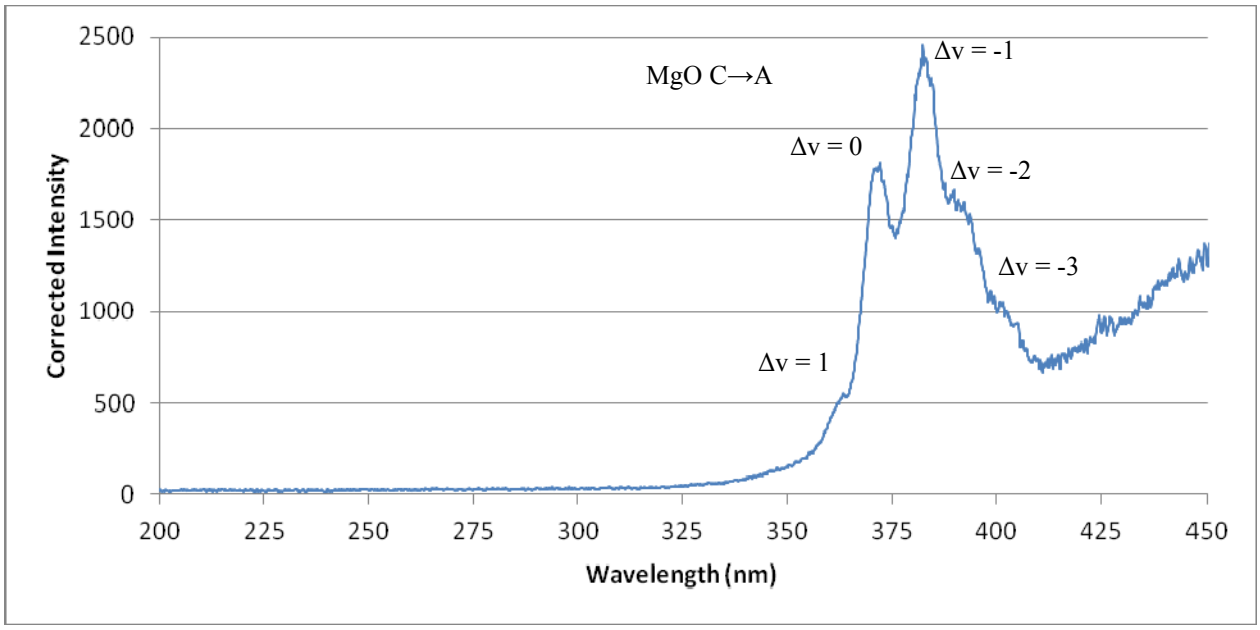

Figure 4.5: Magnesium spectrum (200 – 450 nm) with slit width 90 micron

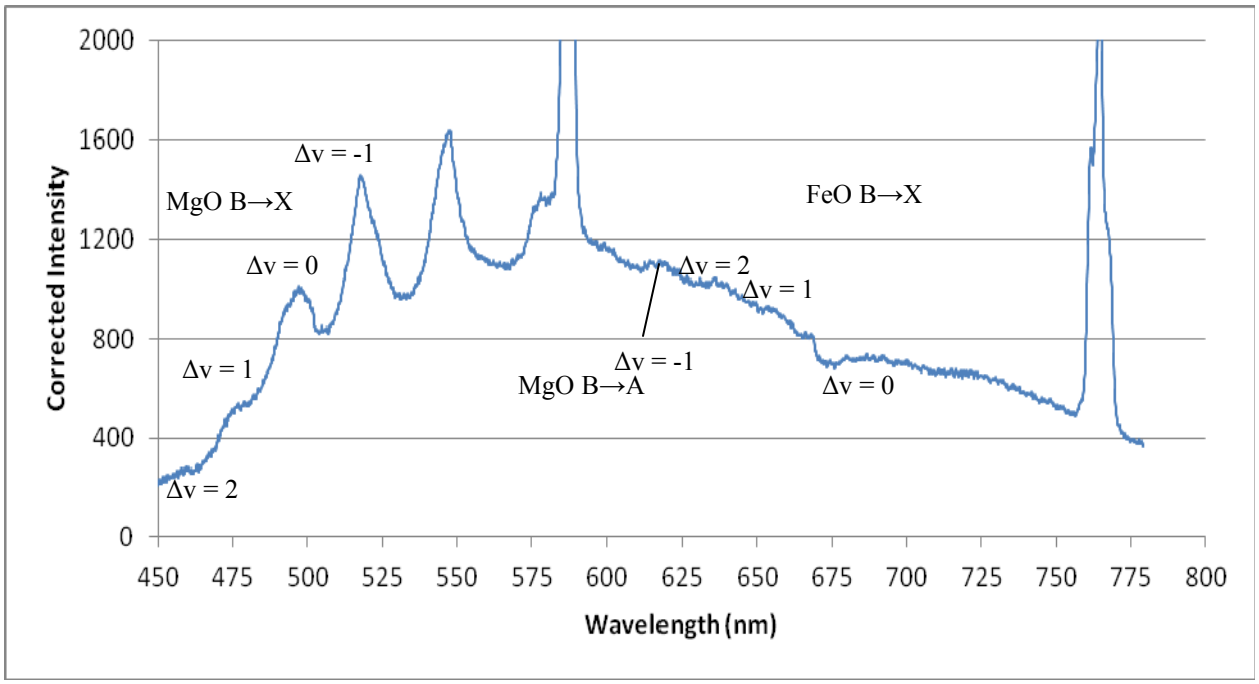

Figure 4.6: Magnesium spectrum (450 – 800 nm) with slit width 70 micron

4.2.4 Hafnium, Zirconium, and Titanium

Three of the metals tested; hafnium, zirconium, and titanium, showed remarkably similar spectroscopic outputs. In all three cases there were no significant features below 450 nm, as shown in Figure 4.7, Figure 4.8, and Figure 4.9. There is a complete absence of visible spectral lines; however, in each case there is a significant amount of noise around 425 nm. This was most likely due to detector noise, as it showed up consistently in almost all tests. Although hafnium and zirconium were of approximately equal brightness, the titanium tested created a significantly brighter image and required the slit size to be reduced all the way down to 40 micron. This was the smallest slit size that was required in all short wavelength tests.

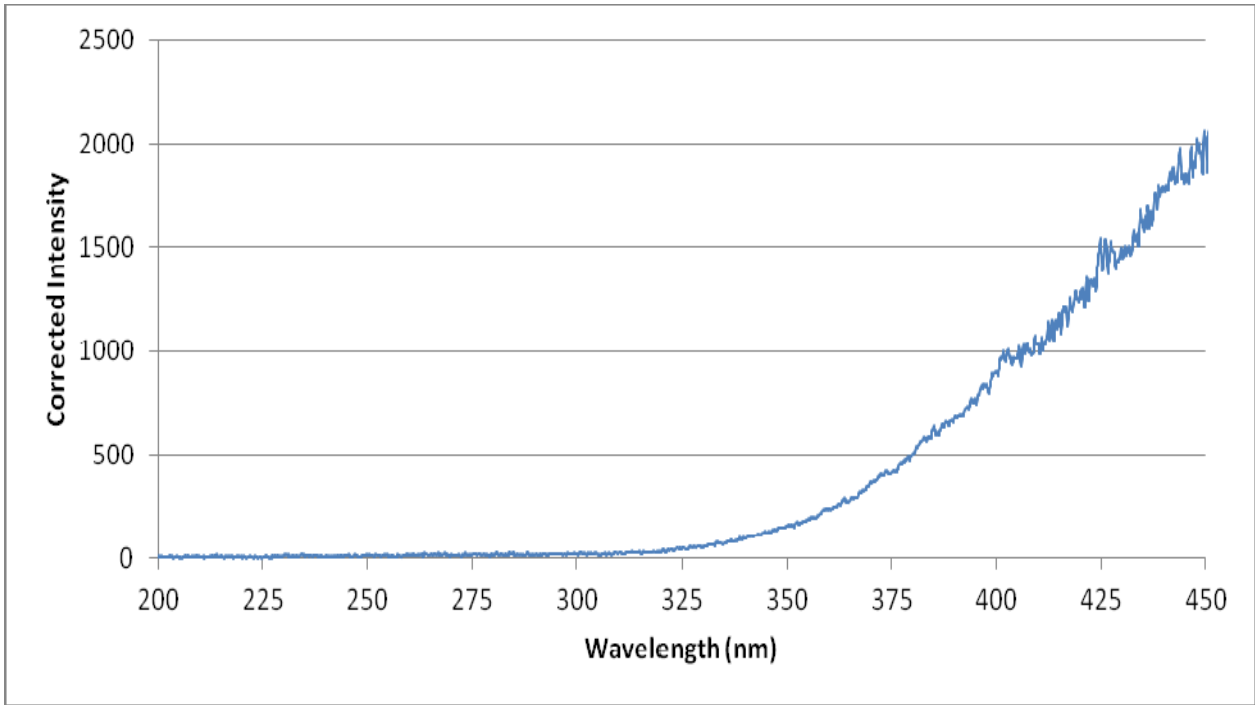

Figure 4.7: Hafnium spectrum (200 – 450 nm) with slit width 90 micron

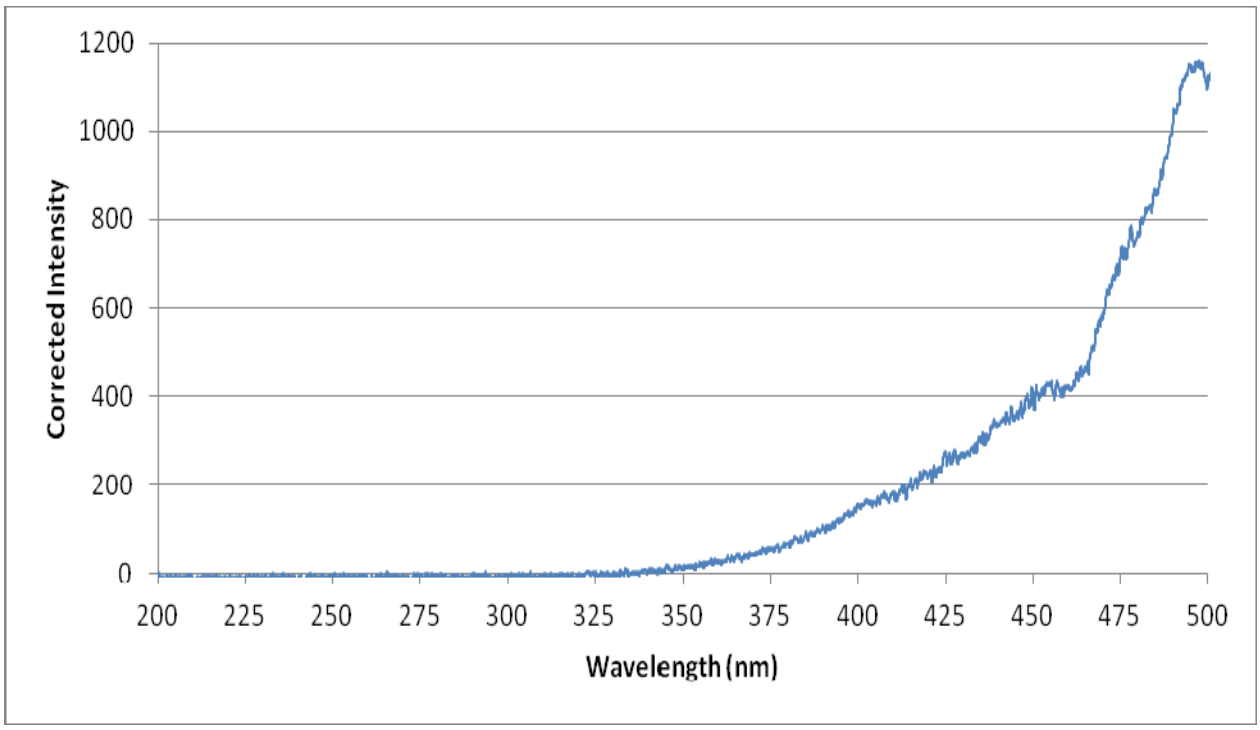

Figure 4.8: Zirconium spectrum (200 – 450 nm) with slit width 90 micron

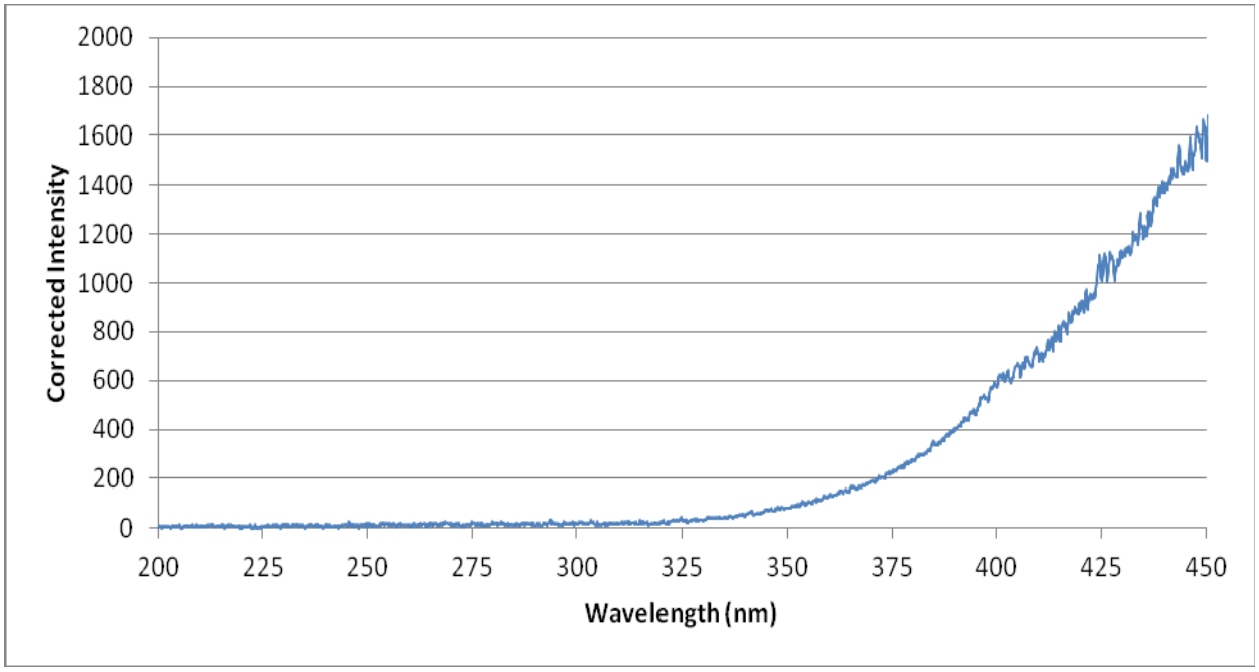

Figure 4.9: Titanium spectrum (200 – 450 nm) with slit width 40 micron

The high wavelength region testing of hafnium, zirconium, and titanium also yielded incredibly similar results, and spectra are shown in Figure 4.10, Figure 4.11, and Figure 4.12. In all cases both the sodium and potassium doublets (588 and 764 nm) are clearly visible, indicating a small impurity of these two substances in each of the powders. Next, each powder shows a weak spectral output at approximately 515 and 547 nm. This series of weak humps is caused by the production of metal oxides in each test. There is no evidence of any molecular emission in any of these metals tested. This series of weak humps is not related to the combustion of any metal, and would disappear if an intensity calibration was performed.

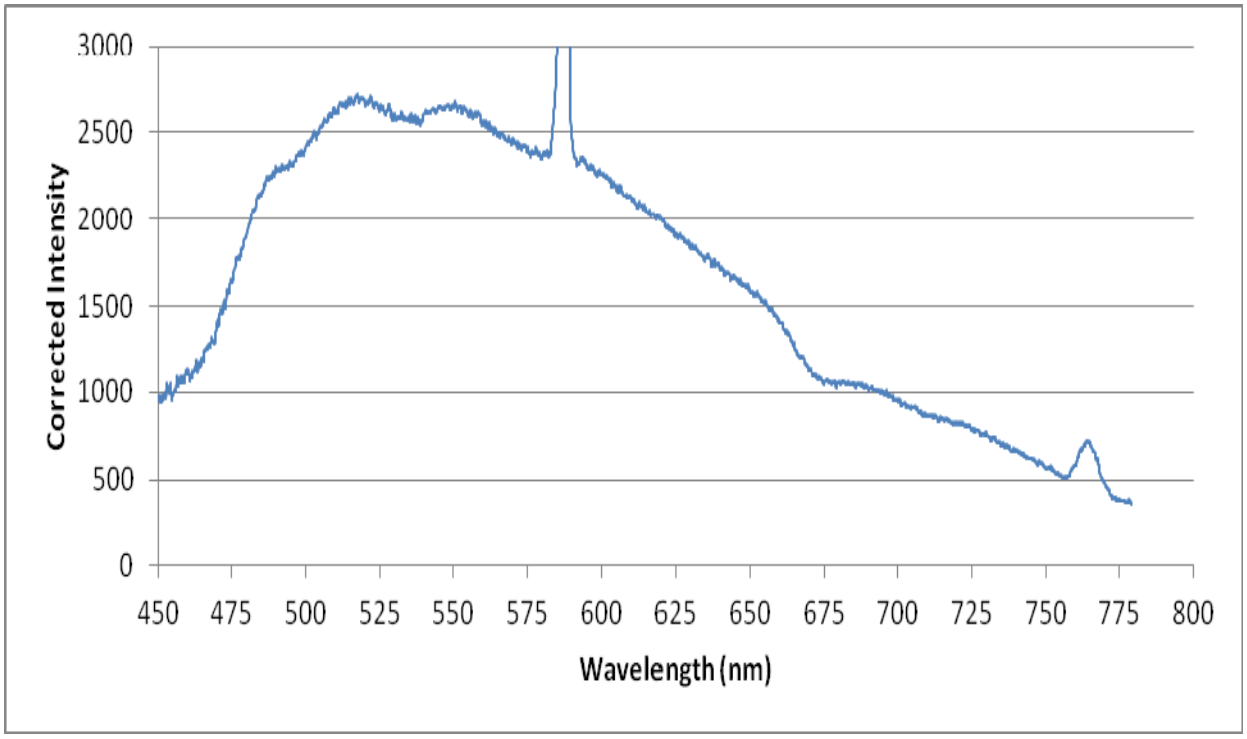

Figure 4.10: Hafnium spectrum (450 – 800 nm) with slit width 30 micron

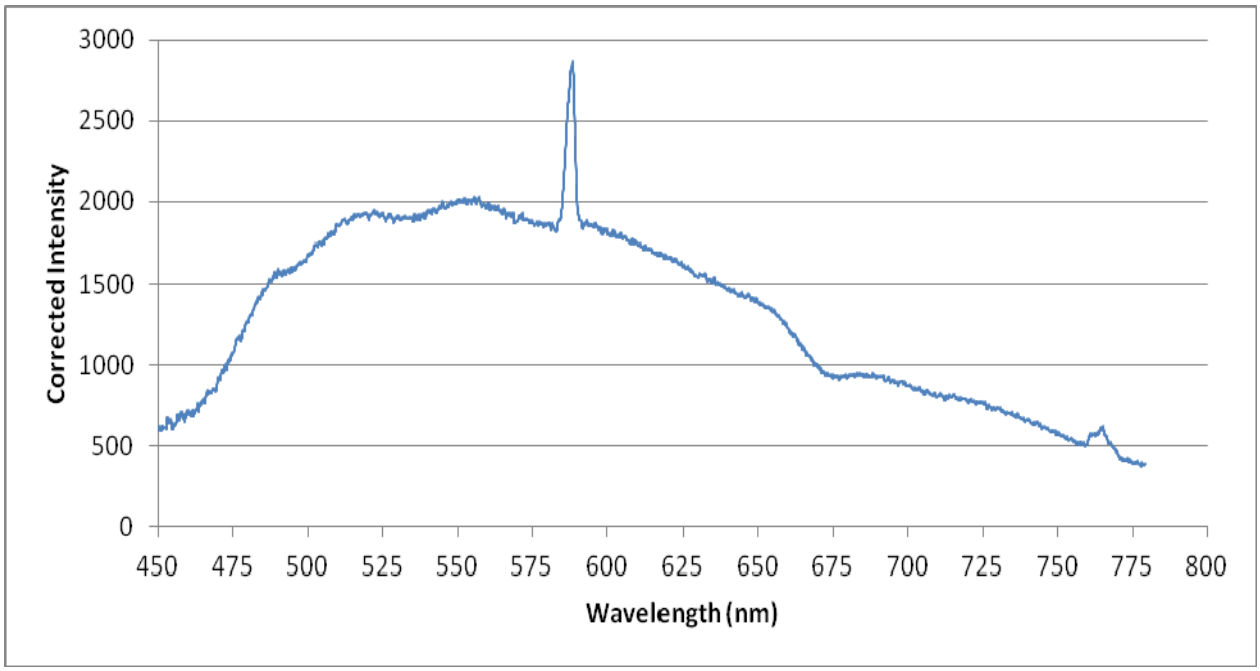

Figure 4.11: Zirconium spectrum (450 – 800 nm) with slit width 70 micron

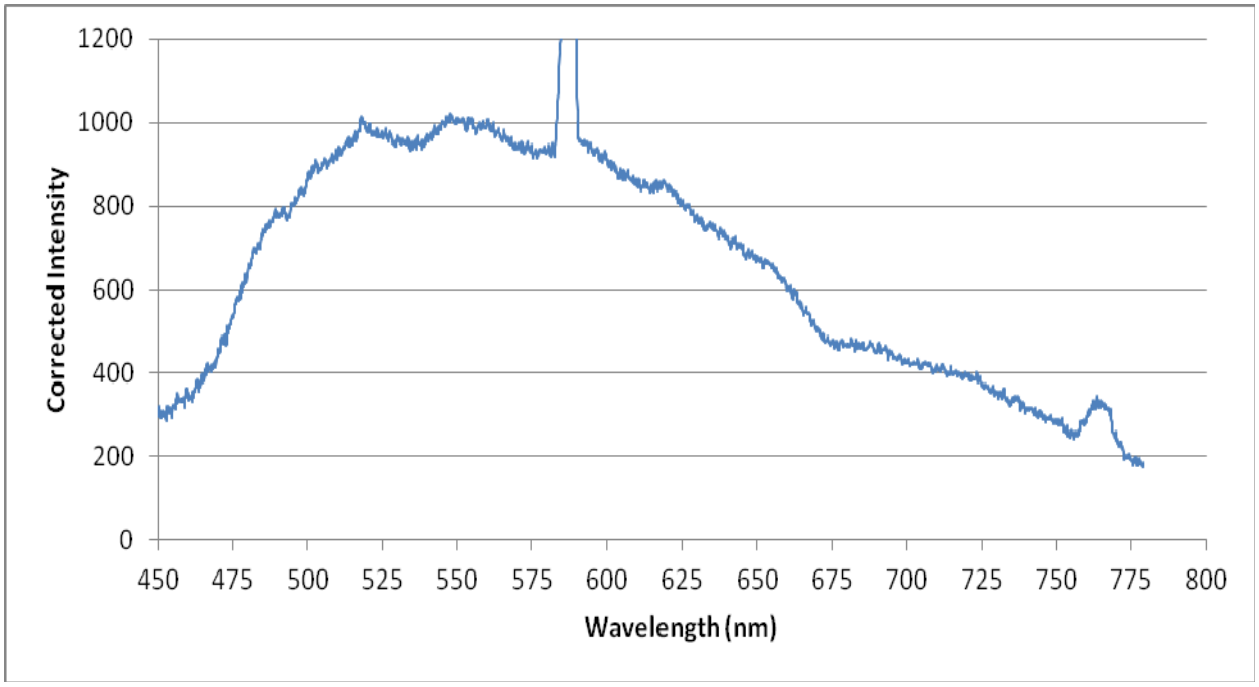

Figure 4.12: Titanium spectrum (450 – 800 nm) with slit width 25 micron

The striking similarities between the three sets of plots can be explained by the Glassman's criterion. When a metal undergoes heterogeneous burning, it does not show gas phase intermediates. Only the thermal features from the hot metal and the resultant oxides are seen. This surface combustion results in a spectral image that appears mostly continuous with few to no discrete features. Each of the three metals in the section burn in a clearly heterogeneous fashion and show no clearly defined peaks, aside from the sodium d-line and potassium doublet. This indicates that the metals have a boiling point that is higher than the volatilization temperature of the metal oxide that they produce. In surface combustion there is no gas phase intermediate, which creates less molecular signature. For zirconium, the metal's boiling point, ~4650 K [26], is higher than the zirconium oxide (Z_2O_3) volatilization temperature, 4280 K [9]. This intuitively creates the continuous spectra shown in the previous figures. Titanium is an interesting case because the metal's boiling point, ~3500 K [26], is fairly close to the metal oxide (Ti_3O_5) volatilization temperature, ~4000 K [9]. This is evident in the plot because the spectral features of titanium monoxide are starting to form and are the most defined of the three metals tested.

4.2.5 Manganese

The results yielded from the manganese tests were fairly straightforward and agreed with documented spectroscopy data. The short wavelength test of the manganese consistently resulted in one peak at a wavelength of 403 nm, which is shown in Figure 4.13. This can be explained by a manganese doublet that occurs between the wavelengths 403.3 and 403.4 nm. The high wavelength region of manganese testing, shown in Figure 4.14, also yielded fairly intuitive results. The brightest feature was once again the sodium D-line (588 nm), caused by a small sodium impurity in the powder. Also visible is the potassium doublet that occurs at 764 nm. The most notable feature relevant to the manganese itself are the peaks at 520, 537, 540, 559, and 620 nm. This series of peaks is caused by the production of manganese monoxide from the $A^6\Sigma \rightarrow X^6\ \Sigma$ transition. The peak for $\Delta v=-2$ is hidden by the sodium D-line that occurs at the same wavelength.

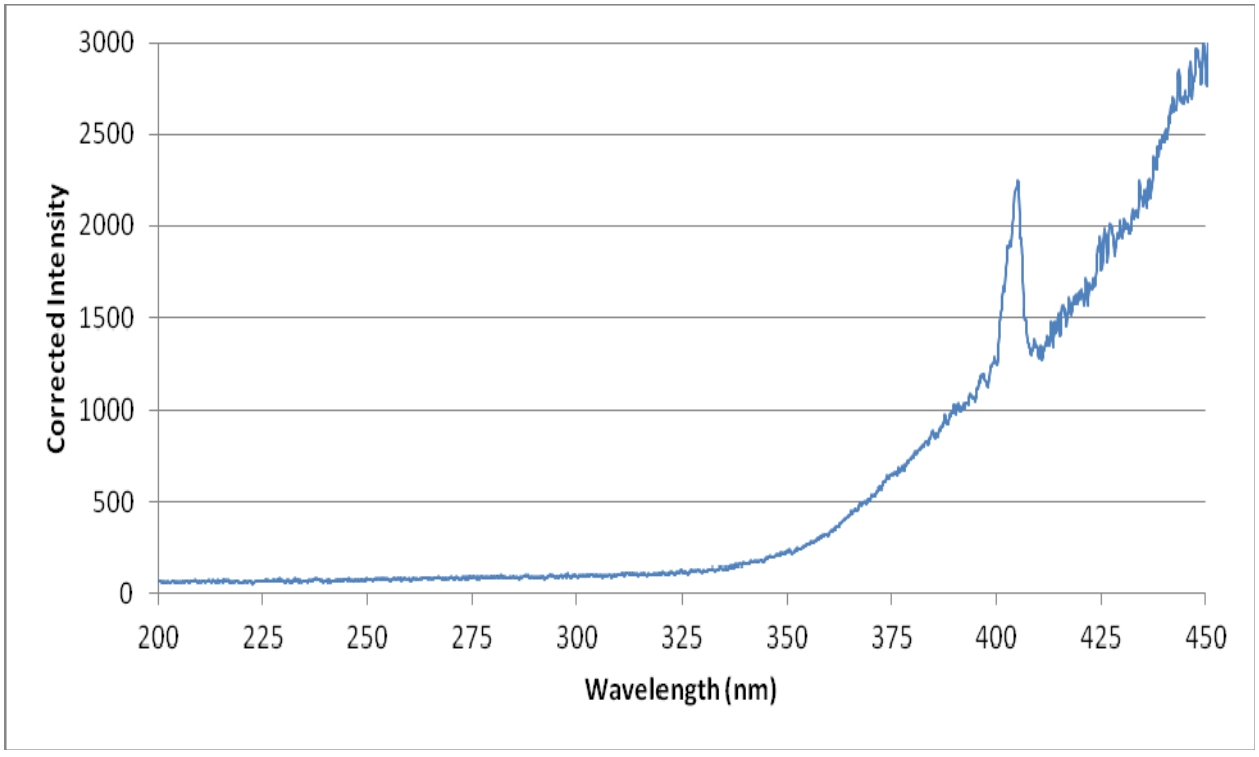

Figure 4.13: Manganese spectrum (200 – 450 nm) with slit width 70 micron

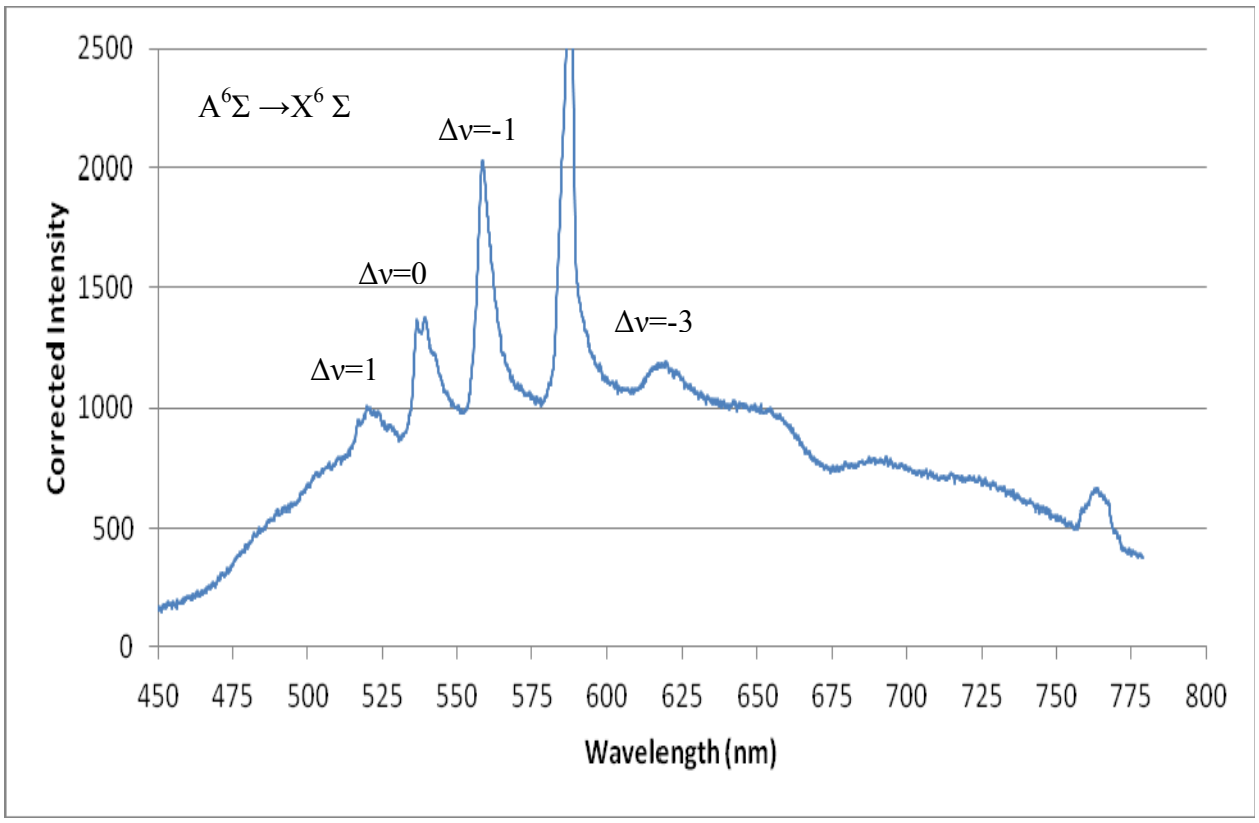

Figure 4.14: Manganese spectrum (450 – 800 nm) with slit width 30 micron

The large number of well-defined manganese monoxide features present in the spectra displayed above indicates that the metal burns homogeneously in air. Upon comparing the boiling point of manganese, ~2235 K [26], with the volatilization temperature of Mn_2O_3, ~3120 K [31], Glassman's criterion confirms that manganese should burn in a homogeneous fashion.

4.2.6 Strontium Chloride

Strontium chloride yielded the most interesting graph in terms of number of relevant features. Strontium chloride was the only compound tested, which is because strontium by itself is highly unstable. This difference creates some challenges in analysis because the number of prevalent possibilities for species is much greater. The first emission to look for is strontium chloride (SrCl) itself. In the high wavelength tests a significant amount of strontium chloride features can be seen. A band centered around 631 nm exists, which represents the $B^2\Sigma^+ \rightarrow X^2\ \Sigma^+$ transition. This band ranges from 603 nm to 722 nm in this experiment. Although it is theorized strontium oxide occurs here, the strontium could react with excess water vapor in the tube, creating strontium hydroxide, or SrOH. The resultant features between 643 and 722 nm resemble the spectral lines of strontium hydroxide. It is difficult to determine which species exists in this range; however, the difference in intensities may indicates that strontium hydroxide may occur in the region instead of strontium oxide.

Another possible product is strontium oxide, or SrO. Strontium chloride (SrCl) is unstable at high temperatures and dissociates into strontium and chlorine. The strontium then reacts with oxygen to create strontium oxides. In the low wavelength region of testing a weak peak at 401 nm occurred which can be explained by the strontium monoxide B→X transition. The chlorine also oxidizes but does not show any significant features in this experiment. In addition to strontium chloride and strontium monoxide features there is a strontium emission shown at 463 nm. Also seen in these plots are the potassium and sodium doublets at 588 nm and 764 nm, respectively.

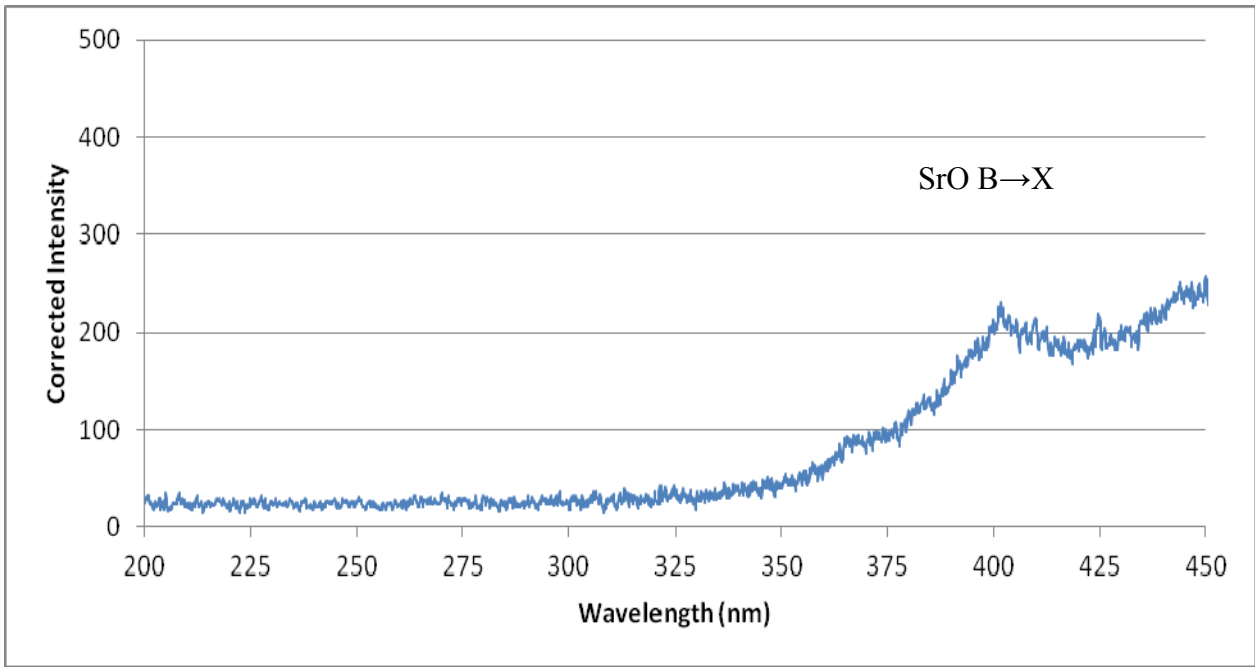

Figure 4.15: Strontium Chloride spectrum (200 – 450 nm) with slit width 70 micron

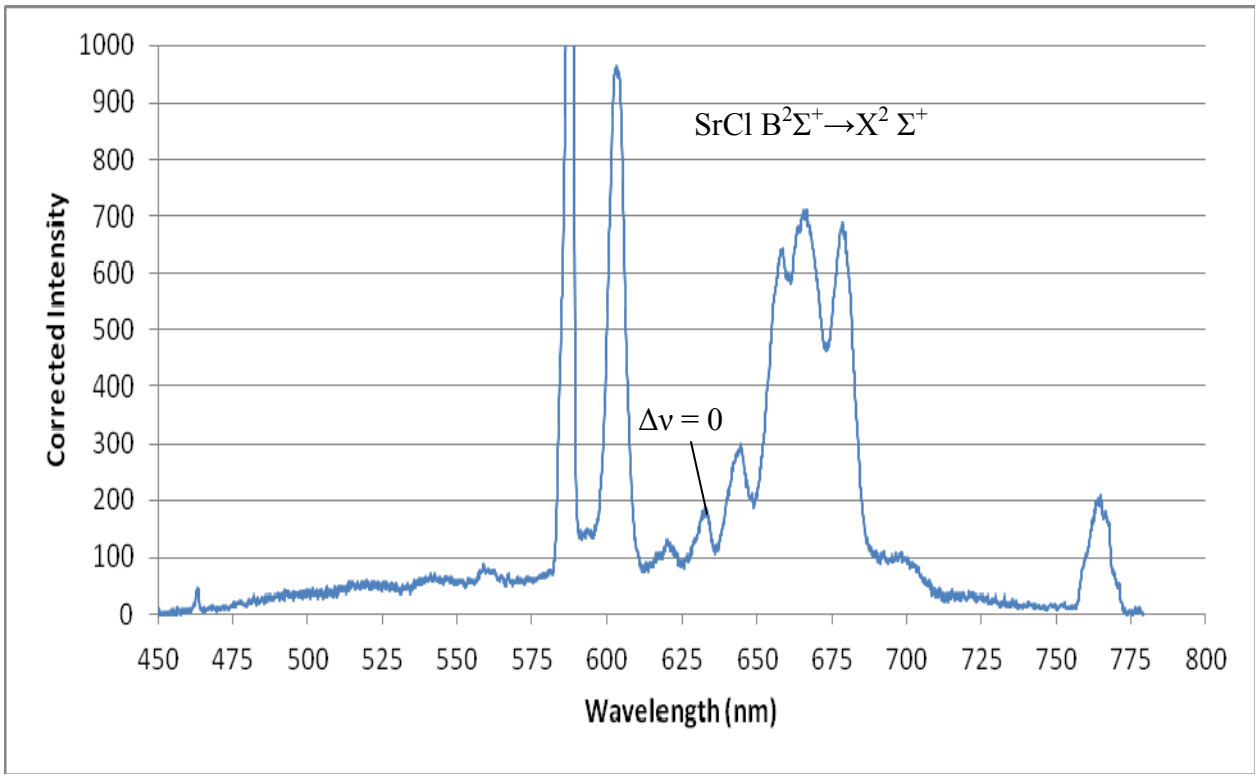

Figure 4.16: Strontium Chloride spectrum (450 – 800 nm) with slit width 25 micron

4.2.7 Silicon

Silicon was a challenging metal to analyze because the silicon monoxide emits at low wavelengths, less than 300 nm [28]. Si_2O_3 and SiO_2 do not emit in this region, according to the NIST website. This indicates that the emissions must come a product that does not result from simple combustion. SiN_2 is one possible product due to silicon reacting with nitrogen in the air. It was found this product emits in the range of 331 to 368 nm [28], which might explain some of the smaller peaks and noise present in that region. Another possible product is SiN, which undergoes a B→X transition centered around 404 nm, and emits at 374, 388, 404, 421, and 441 nm. There is evidence of features at these locations, however they are not well defined.

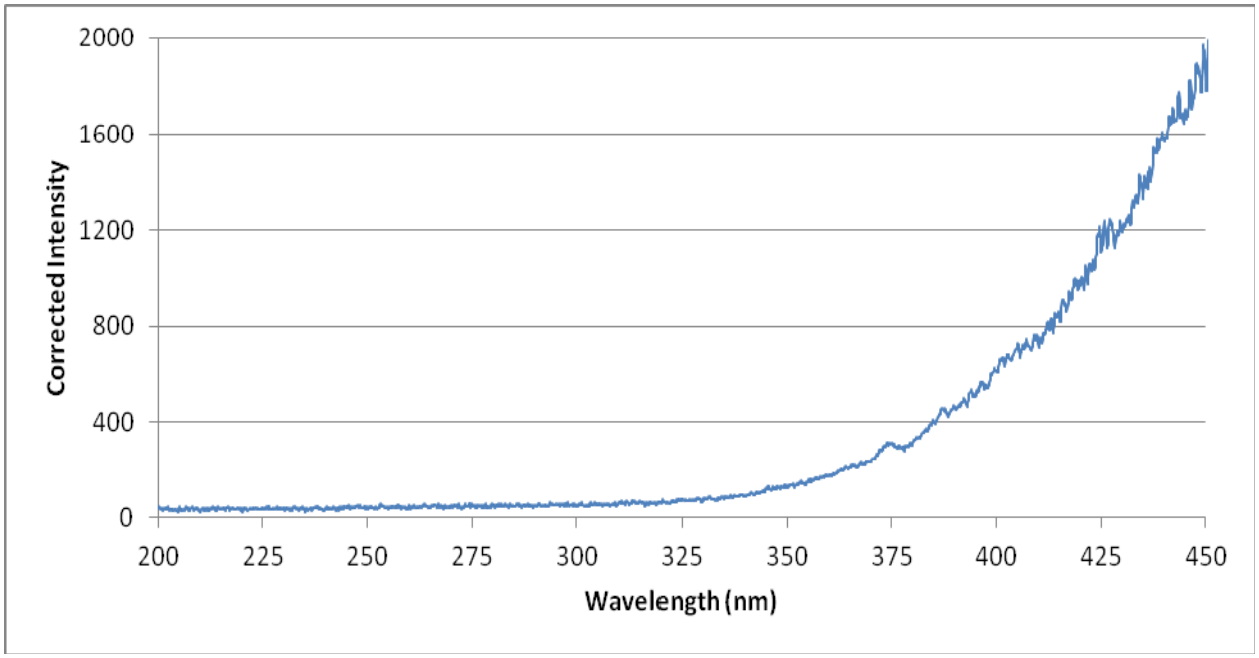

Figure 4.17: Silicon spectrum (200 – 450 nm) with slit width 90 micron

For the longer wavelengths, the spectroscopic output was once again difficult to analyze due to the absence of silicon oxides. The features between 600 and 700 nm can be explained by the iron oxide impurity that has been explained in depth in previous sections and the sodium d-

line and potassium doublet are well defined; however, it is difficult to analyze the features between 475 and 550 nm. One possible source for these features is the SiN B→X Δv = -4, -5, -6 transition. Another possible source for the 519 nm peak is an Si_3 transition combined with a moderate Si I transmission at 500 and 549 nm. Neither of these solutions seems very likely so the peaks are most likely coming from an unknown source.

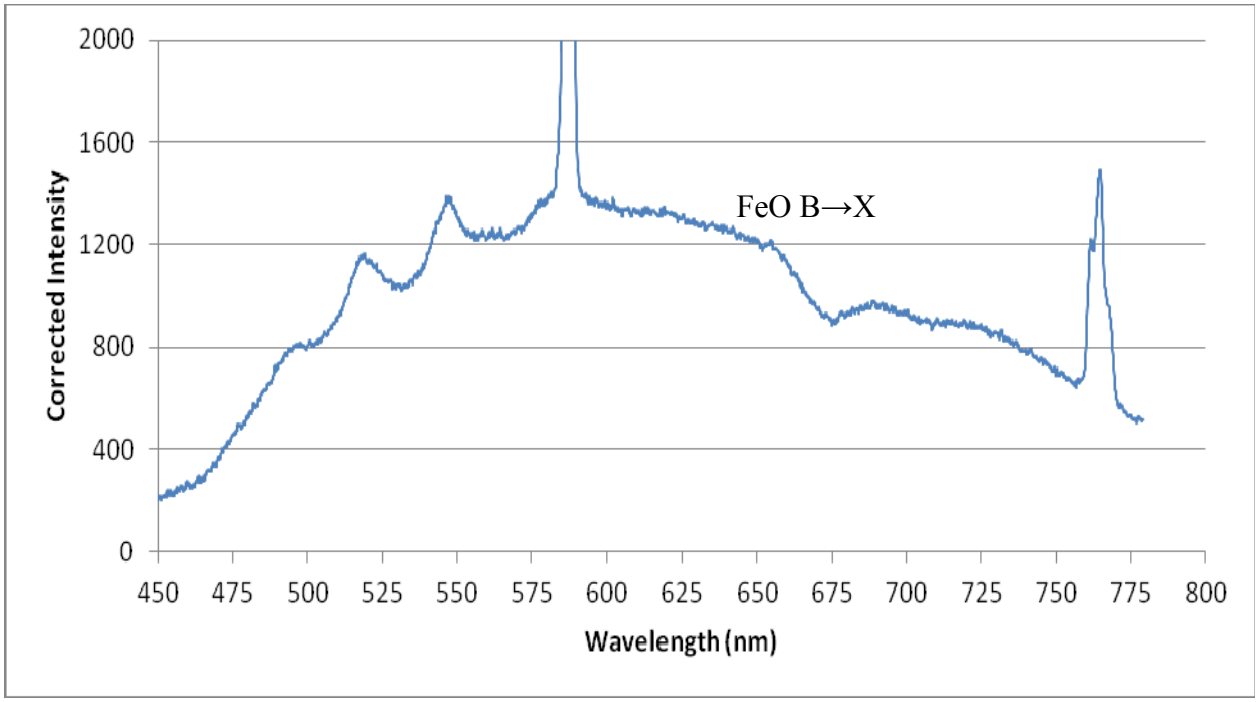

Figure 4.18: Silicon spectrum (450 – 800 nm) with slit width 50 micron

The spectrum that results from the silicon tests looks quite similar to that of the hafnium, zirconium, and titanium sections. This similarity is caused by the heterogeneous nature of the silicon burning. The boiling point of silicon is approximately 3100 K [26] whereas the combustion temperature of SiO_2 is only ~2503 K [31]. Since the combustion temperature of the silicon dioxide is significantly lower than the boiling point of the silicon, this particular series undergoes heterogeneous burning in this region. This indicates mainly surface combustion occurs and results in a poorly defined spectral output.

4.2.8 Scandium

Little shock tube experimentation has been completed to date on scandium, although it is very energetic. One of the initial problems with testing the scandium was the powder did not have a documented maximum particle size like the other materials tested. To solve this problem, the powder received was ball milled and ground to a finer powder before use. Another problem encountered with the scandium powder involved the analysis of the data. The spectroscopic output of scandium was slightly more challenging to analyze because scandium oxide appears at a multitude of wavelengths. This makes it difficult to determine if the features shown in the test results are a result of the scandium oxides that are created or as a result of some other influences. A third problem with running the scandium powder was the inconsistency of ignition. During certain tests the powder would not ignite adequately and only the sodium D-line would be present. This inconsistency is most likely due to the non-uniformity of the powder used. Different particle sizes ignite differently and, since only a small amount of powder was used for each test, this inconsistency caused different outputs.

The low wavelength region of the scandium powder, shown in Figure 4.19, did not show any interesting features, whereas the section of longer wavelengths showed several significant peaks. The particularily strong emission at 464 nm does not correspond to any known features of scandium or its compounds. The closest compound is Sc_4, which occurs at 451 nm [28]; however, this seems like an unlikely source for the feature. This peak is probably caused by an impurity in the experimental setup or in the powder. The features between 475 and 550 nm were difficult to analyze because the individual peaks were not well defined and difficult to resolve. Literature suggests a ScO $B^2\Sigma^+ \rightarrow X^2\Sigma^+$ transition centered around 476 nm that includes a peak at

476, 496, and 518 nm [28]. While this is not perfectly defined in the image, this ScO transition is the only one that exists in this region.

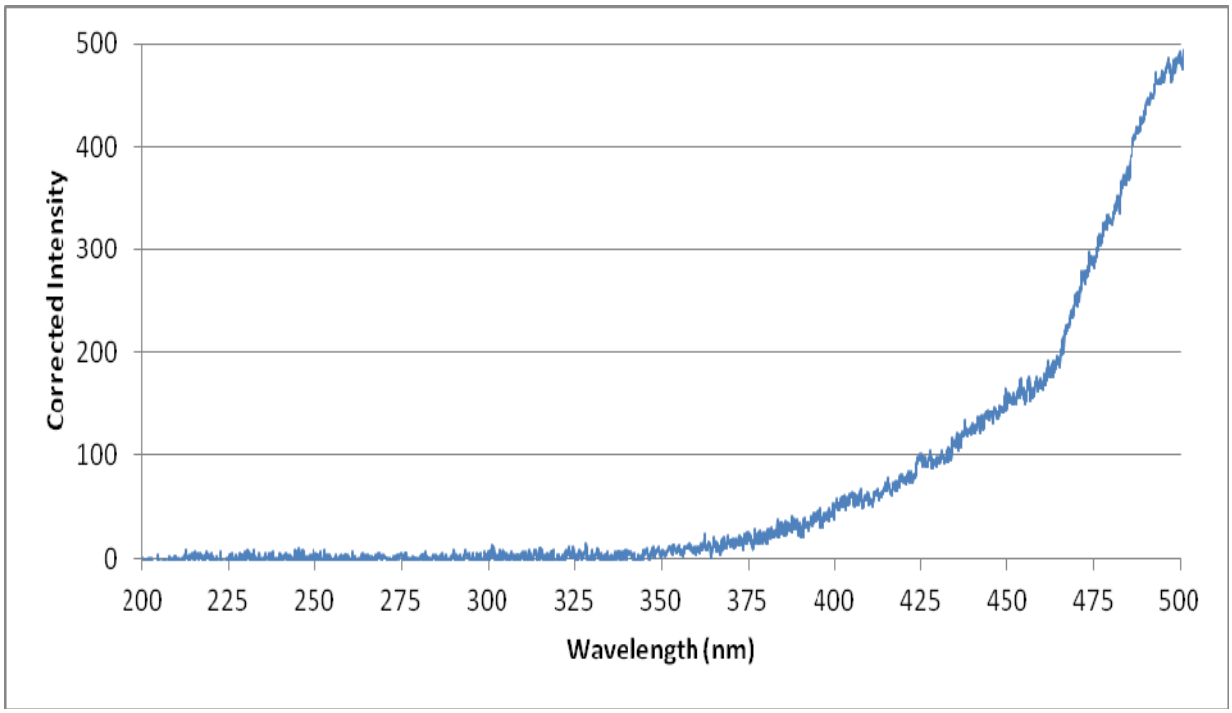

Figure 4.19: Scandium Spectrum (200 – 450 nm) with slit width 110 micron

The next series of peaks (560 – 680 nm) can be described mainly by two variations of the A→X transition. The first transition series, A→X, is centered around 588 nm, explains the peaks located at 560, 588, 620, and 656 nm. The second transition suggested by literature is an A'→X transition centered around 642 nm and encompasses the 580, 610, 642, and 679 nm peaks. These two transitions match the spectroscopic images collected during the scandium but there are also other possible explanations for the various features. At 588 nm, the peak may also be caused by the sodium D-line which consistently showed up in every test. Also, the shape of the plot between 630 and 700 nm matches other metals very closely, which may indicate these features may actually be caused by the iron impurity that has been identified in the shock tube.

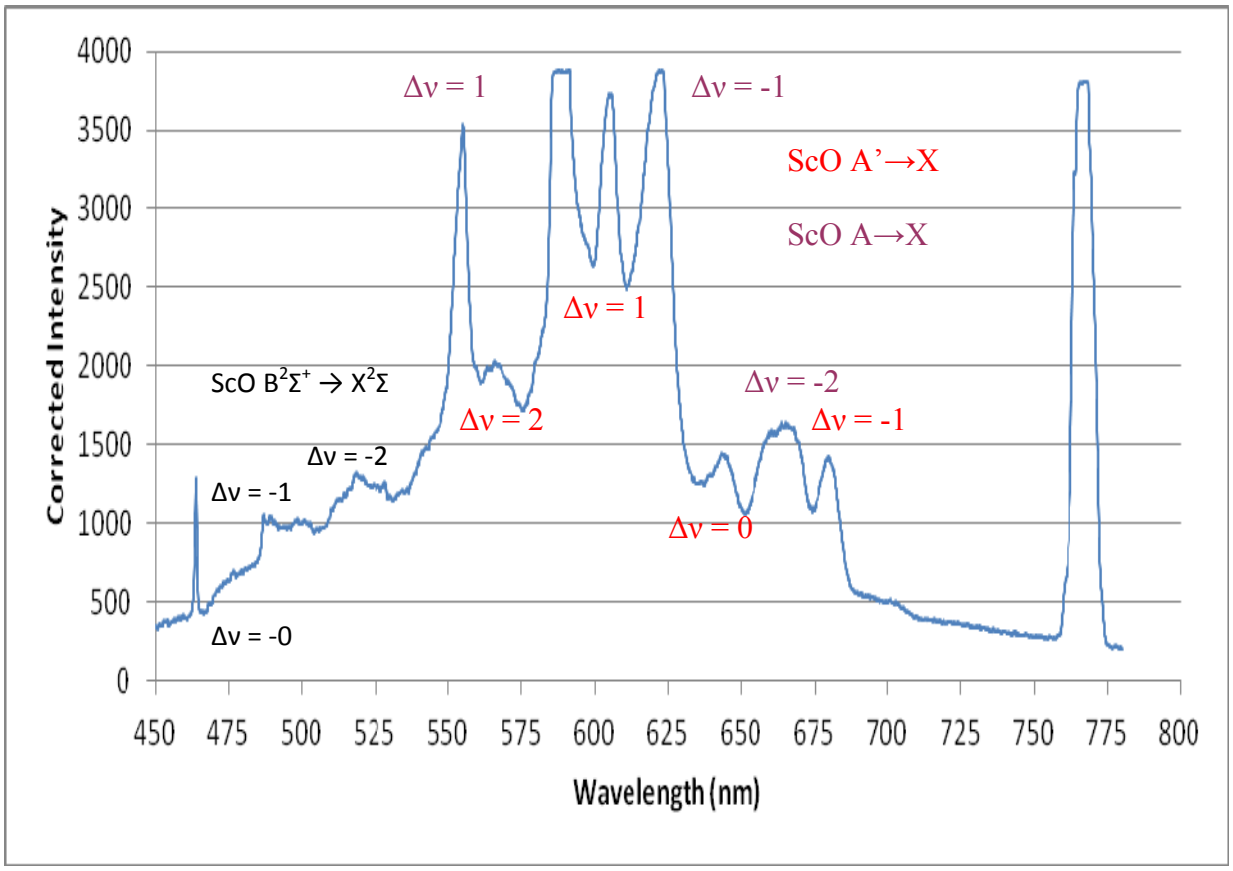

Figure 4.20: Scandium Spectrum (450 – 800 nm) with slit width 50 micron

5. Conclusion and Recommendations

5.1 Conclusion

There were two primary goals of this experiment: improve the overall quality of the shock apparatus by repairing leaking features and to collect the spectroscopic outputs of various energetic metals. The first goal was achieved by isolating sections of the shock tube and leak testing components until the endwall and manifold sections were identified as sources of significant leaking. These sections were redesigned decreased the amount of pressure lost in 90 seconds from ~5 psi to ~0.1 psi. The second goal was accomplished using the improved shock tube setup and its results can be summarized as follows:

- The overall quality of the experimental setup was confirmed by a baseline aluminum test. The AlO $B^2\Sigma^+ \rightarrow X^2\Sigma^+$ transition centered about 473 nm was observed and matched previous documentation. The sodium D-line and potassium were also seen in their correct locations (588 and 764 nm, respectively) and an iron impurity was located in the tube. This impurity yielded iron emission signatures at 644 and 666 nm, as well as the FeO $B \rightarrow X$ transition centered about 679 nm. This experiment confirms that aluminum burns homogeneously.
- Boron tests yielded similar results to published data. The BO_2 $B^2\Sigma \rightarrow X^2\Pi$ transition was located at 409 nm in addition to the BO_2 $A^2\Pi \rightarrow X^2\Pi$ transition between 454 and 637 nm. The BO $A^2\Pi \rightarrow X^2\Pi$ transition was also observed at 416 and 438 nm. B_2O_3 was not observed in the range shown. The second stage of boron combustion (bare boron particle combustion) was witnessed.

- Magnesium tests yielded the most prominent features below 400 nm, correlating to the MgO C→A transition and the magnesium triplet. Magnesium emission was also seen at 548 nm. At 591 and 691 nm, parts of the MgO B→A can be seen, even though the 591 nm peak is overshadowed by the sodium D-line at 588 nm. The MgO $B^1\Sigma^+ \rightarrow X^1\Sigma^+$ transition, centered around 490 nm, was also observed. The FeO B→X was once again seen between 625 and 700 nm. Magnesium underwent heterogeneous burning.
- Hafnium, zirconium, and titanium all yielded similar results because they burn heterogeneously. This type of burning, surface combustion, shows a minimal amount of spectroscopic features.
- Manganese showed a strong spectrum of spectral lines and matched documented results quite accurately. The MnO $A^6\ \Sigma \rightarrow X^6\ \Sigma$ transition centered around 546 nm was present, including the spectral lines at 525, 546, 570, and 620 nm. Manganese also burns homogeneously, as evident by its clear spectral features.
- Silicon showed many of the same features as the hafnium, zirconium, titanium group but its peaks were more refined. Silicon was determined to burn heterogeneously, however, it was still feasible to resolve the features. Products that show up in the spectrum were determined to be SiN_2, SiN, and FeO; whereas SiO and SiO_2 were not observed. SiO was theorized to occur at <300 nm, but experimental constraints inhibited these lines. SiN_2 may have been seen between 331 and 368 nm, but once again experimental constraints inhibited these. SiN was observed between 374 and 441 nm. Once again, the iron impurity was observed between 600 and 700 nm, as well as the sodium D-line and potassium doublet.

- Strontium Chloride was the only molecule tested due to strontium's unstable nature. SrO B→X emission was identified at 401 nm and strontium emission was shown at 463 nm. In addition to strontium monoxide, SrCl emission was identified via the $B^2\Sigma^+ \rightarrow X^2\Sigma^+$ transition centered around 631 nm. The sodium D-line and potassium doublet were also identified. Strontium was also identified to burn homogeneously.
- The least documented metal tested was scandium, which emitted at several wavelengths. Several ScO emissions were identified during this experiment, including the B→X transition centered around 476 nm, the A→X transition centered around 588 nm, and the A'→X transition centered around 642 nm. There also were features that appeared quite similar to the iron impurity documented in other tests.

5.2 Recommendations

There are a couple of recommendations to improve the experiments that have arisen from these tests. The first couple things involve upgrading the equipment that the shock tube currently operates with. First, the camera used only offered a low range of intensities and oftentimes experiments had to be re-run in order for the spectrum to come up clear and not fully saturated If experimentation is to be done without altering the slit opening on the spectrometer a camera with a larger range of intensities is necessary. Aside from the optics setup, some of the hardware in the shock tube is starting to fail. The set screws in the endwall section started to strip towards the end of experimentation and the bolts connecting the driver section became increasingly difficult to remove. The latter problem may be caused by the shock tube itself being slightly off alignment. The most obvious improvement to be made on the shock tube is to remove the iron impurity from the inside of the tube, which may not be feasible. The next couple recommendations involve the experiments themselves. Several metals proved to be promising based on their spectroscopic outputs and more tests should be conducted in various environments and temperatures. For example, strontium and manganese looked promising; and little is currently known about scandium and its applications. In addition to expanding the test parameters of metals tested in this study, further examination into compounds and alloys of these metals should be examined as well. A third suggestion for improving the experiment is to unify the types of powders tested and their masses. By using powders of all the same size and in the same quantities, more quantitative data can be acquired from the experiments. In addition, these new powders should be of higher purity in an attempt to limit the number of impurities that are present in the data.

References

1. Oosthuizen, P.H., and Carscallen, W.E., 1997, *Compressible Fluid Flow*, p 36, 77-79, 82-83, 103-105.

2. Lynch, P. *High Temperature Spectroscopic Measurements of Aluminum Combustion in a Heterogeneous Shock Tube.* University of Illinois at Urbana-Champaign, 2010.

3. Gaydon, A.G., and Hurle, I.R., *The Shock Tube in High Temperature Chemical Physics*, Chapman and Hall, London, 1963.

4. *Shock Tube Operation*, Rensselaer Polytechnic Institute. http://www.eng.rpi.edu/mane/lightcraft/Curriculum/Experimental/ShockTube/elements_1.html. 18 November 2010.

5. Atkins, P. and De Paula, J. *Physical Chemistry 8th Edition*. Freeman Publishing, New York, NY. 2006.

6. Grosse, A.V. and Conway, J.B.. *Combustion of Metals in Oxygen*. Research Institute, Temple University, Philadelphia, PA. 1958.

7. Brown, Jon., 2007, *Comparison of Ignition Characteristics of Pure and Coated Aluminum Powder in a Shock Tube Facility*. University of Illinois at Urbana-Champaign

8. Glassman, I. American Rocket Society, ARS Reprint No. 938-959. New York, 1959.

9. Glassman, I and Yetter, R.A. *Combustion 4th Edition*. Elsevier Inc., USA. 2008

10. Mavrodiuneanu, R. and Boileux, H., *Flame Spectroscopy*. John Wiley and Sons, New York, NY, 1965.

11. Laurenduea, N.M., *Statistical Thermodynamics: Fundamentals and Applications.* Cambridge University Press, New York, NY, 2006

12. Servaites, J. *Combustions of Aluminum Particles in Rocket Motor Oxidizers Within a Shock Tube.* Masters Thesis. University of Illinois at Urbana-Champaign, 2001.

13. Hok, H. *A Laser Scanning Technique for Measuring Solid Propellant Burning Rates.* University of Illinois at Urbana-Champaign. Masters Thesis. 1997.

14. Bazyn, Timothy. *Spectroscopic Measurements of the Combustion of Aluminum and Aluminum-Based Energetic Material Particles Using a Heterogeneous Shock Tube.* PhD Dissertation. University of Illinois at Urbana-Champaign, 2006

15. Sutton, G.P. *Rocket Propulsion Elements ed. 7*. John Wiley and Sons, New York, NY. 2001.

16. Krier, H., *Ignition Dynamics of Boron Particles in a Shock Tube*. Journal of Propulsion and Power Vol. 14, No. 2, March – April 1998.

17. Krier, H. *Shock Initiation of Crystalline Boron in Oxygen and Fluorine Compounds*. Journal of Propulsion and Power, Vol. 12, No. 4. July – August 1996

18. *Advanced Energetic Materials*. National Research Council of the National Academics, National Academic Press, Washington DC, 2004. pg. 20-23.

19. Vadine, P, et al. *Cast Aluminized Explosives*. Combustion, Explosives, and Shock Waves, Vol. 44, July – August 2008, pg. 461-477.

20. Orth, L and Krier, H. *Shock Physics for Nonideal Detonations of Metallized Explosions.* 27th Symposium (Intl.) on Combustion. The Combustion Institute, 1998. pg 2327 – 2333.

21. Goroshin, S, et al. *Emission Spectroscopy of Flame Fronts in Aluminum Suspensions.* Proceedings of the Combustion Institute 31. 2007

22. N. Eisenreich and W. Liehmann, *Emission Spectroscopy of Boron Ignition and Combustion in the* Range *of 0.2 mm to 5.5 mm*. Propellants, Explosives, Pyrotechnics. 1987. pg 88-91.

23. Spalding, M., *Boron Particle Ignition and Combustion in a Shock Tube Using Time Resolved Spectroscopy.* Masters Thesis. University of Illinois at Urbana-Champaign, 2000.

24. Parker O-Ring Handbook, Parker Hannifin Corporation. Cleveland, OH, 2007

25. Fiore, G. *Temperature Sensitivity Investigation of the AlO Δv = -2 Bands.* Masters Thesis. Politecnico di Milano. 2010.

26. Bentor, Y. *Periodic Table: Boiling Point*. www.chemicalelements.com. 3/20/11.

27. *Spectrum of Magnesium Discharge*. http://astro.u-strasbg.fr/~koppen/discharge/magnesium.html. 3/27/11.

28. NIST Chemistry Webbook. US Secretary of Commerce. http://webbook.nist.gov/chemistry. 4/1/11

29. Gulbransen, E.A., and Janssen, S.A., *The High Temperature Oxidation, Reduction, and Volatilization Reactions of Silicon and Silicon Carbide.* Oxidation of Metals, Vol. 4, No. 3, 1972. pg 184-201.

30. Yeh, C.L. and Kuo, K.K. *Ignition and Combustion of Boron Particles*. Prog. Energy Combust. Sci. Vol. 22. Pp. 511-541, 1996.

31. Aylward, G. and Findlay, T. *SI Chemical Data Book (4th ed.)*. John Wiley & Sons. 1999.

A. Updated Shock Tube II Operating Manual

Shock Tube II Operating Manual

Original by Josh Felts

Revised by Jon Brown 4/9/07

Revised by David Joyce 11/17/10

Cleaning Procedure

1. Remove the test section/endwall from the driven section.
2. Remove what was used to load the powder (injector, plate).
3. Insert the BRCT into the tube with it attached to the rope and spindle.
4. Go into 1308 MEL and open the diaphragm section.
5. Remove and discard the used diaphragms.
6. Insert the vacuum hose into the shock tube driven section.
7. Vacuum out the driven section. This will cause the BRCT to be drawn to that end.
8. Attach the green scrubber cylinder to the rope and pull it back through the tube from 1304 MEL.
9. Repeat steps 3 and 6-8.
10. Repeat steps 3 and 6-7.
11. Attach the yellow chamois cylinder with 2 folded kimwipes aligned in a plus sign shape coated in foaming glass cleaner to the rope and pull through the tube.
12. Repeat step 7.
13. Repeat step 11 using ethyl alcohol instead of glass cleaner.
14. Clean the last few feet of the shock tube with the green scrubber on a stick, covered with a kimwipe held on by tape, and sprayed with glass cleaner.
15. Clean the last few feet of the shock tube with the yellow chamois on a stick sprayed with ethyl alcohol.
16. Remove bits of grime on the test section/endwall with green scrub pad.
17. Clean test section/endwall with foaming glass cleaner.
18. Clean test section/endwall with ethyl alcohol.
19. Use an LED to ensure alignment of mirror and lens is correct.
20. Reinstall the test section/endwall onto the shock tube.
21. If using injector, clean injector using procedure to follow and re-install.

Loading Powder

1. To use the plate loading method, follow the following steps
    a. Clean the plate with alcohol.
    b. Load a small amount of powder in a line along the last ½" of the plate.
    c. Carefully insert the powder into the port trying not to spill any of it
    d. Screw down the retaining plate over the plug
2. To use the injector loading method, follow these steps.
    a. Clean the injector and wipe down with alcohol.
    b. Make sure both valves on the bypass line are open.
    c. Lightly coat the inside of the bore with vacuum grease.
    d. Coat the piston with vacuum grease making sure to get the o-rings.
    e. Insert the piston into the bore.
    f. Install the insert screw into the 12-hole screw.
    g. Fill the insert screw with powder and pack down.
    h. Carefully install the 12-hole screw into the injector tip.
    i. Install two screens on the end of the injector tip.
    j. Install the screen retaining ring.
    k. Attach injector to shock tube adapter plate.
    l. Attach air supply line to injector.
3. To simply load the powder directly into the bottom of the tube
    a. Clean injector tip and all exposed surfaces with alcohol.
    b. Place a small amount of powder directly into the center of the tube via the injector hole.
    c. Attach the injector to the tube (to seal the tube).

Instrumentation Setup

1. Make sure the SpectraArray program on the silver laptop is running and set to trigger.
2. Make sure the pulse generator is set to "high gate" mode and will trigger with a shock.
3. Open PicoScope and ensure all input signals are working.
4. Press the single run button in SpectraArray
5. Press the start button on the pulse generator.
6. Press the run button in PicoScope program

Firing Procedure

1. Examine the inside of the tube to ensure that it has been cleaned. If not proceed to section entitled "Cleaning Procedure".
2. Determine the operating conditions needed for the test, i.e. driver and driven pressures, from the final temperature, pressure, and oxidizer composition dictated by the test. To do this run the STv3.exe code in *My Documents/shock codes/* for shock velocity, driven pressure, and driven composition. Repeat until desired test conditions are reached.
3. To get driver pressure refer to past runs for the same driven composition for trends in shock velocities to get an educated guess for the pressure.
4. To get diaphragm pressure, add 14.7 psi to driver pressure, divide total by 2, and subtract 14.7 psi to get the gauge pressure. It is generally half of the driver pressure.
5. Select appropriate size/quantity of diaphragms to hold back the diaphragm pressure. Thick diaphragms hold ~200 psi.
6. Proceed into 1308 MEL to install the diaphragms. This is done by first unbolting then opening the diaphragm section and removing the used diaphragms. Next mark and punch the holes in the diaphragms and place them over the pins on each side of the section. Close section and tighten the bolts.
7. Return to 1304 MEL making sure the door is locked to 1308 MEL and the red testing light is on.
8. Load powder via the appropriate method detailed in the "Loading Powder" section.
9. Turn the power on for the control panel.
10. Turn the "shock tube vent" valve to the closed (no) position.
11. Open both green valves on the shock tube, open the black valve on the vacuum pump, and turn on the power for the vacuum pump.
12. When the vacuum gauge reaches its minimum (approximately -28.7 in Hg), purge with 25-50 torr of argon (if testing with a desired composition and not just air).
13. Repeat step 12.
14. Turn on valve for bottle H-1 of helium on the control panel.
15. Set regulator pressure at slightly greater than required diaphragm pressure
16. Slowly crack open "pressurize diaphragm" valve.
17. Fill diaphragm section to desired pressure.

18. Close “pressurize diaphragm” valve.
19. Set regulator pressure at slightly greater than required driver pressure.
20. Select either the 0-200 or 0-1000 psi gauge to measure driver pressure.
21. Slowly crack open “pressurize driver” valve.
22. Fill driver section to desired pressure.
23. Close green vacuum pump valve and turn of vacuum.
24. Fill driven section with appropriate composition of gases using manifold on control panel. Fill with inert first then oxidizer.
25. Close green valve on driven section of tube.
26. Make sure all measurement instruments are ready to go. This procedure is illustrated in the “Instrumentation Setup” section.
27. Recheck driver pressure and fill back up if needed.
28. Make sure the four valves at the bottom of the control panel are all in the closed (no, fire) position.
29. Warn everyone in rooms 1308 and 1304 MEL of the impending test.
30. Turn off room lights.
31. Flip the “Ready to Fire” switch into the yes position. Light will come on.
32. This should trigger scope4pc program, so reset the trigger by pressing “single.”
33. If using the injector method for loading powder, close valve closest to injector just prior to firing, and then flip the switch to inject the powder.
34. Turn the “Fire” knob counterclockwise to fire the tube.
35. Run complete. Save data before touching any equipment.
36. Turn the “Fire” knob all the way clockwise and flip the “Ready to Fire” switch to the no position.
37. Open the “Shock Tube Vent” valve and the black valve on the driven section of the tube to vent out gases to the exhaust.
38. Turn off Control Panel.

B. Detailed Drawing of Designed Endwall

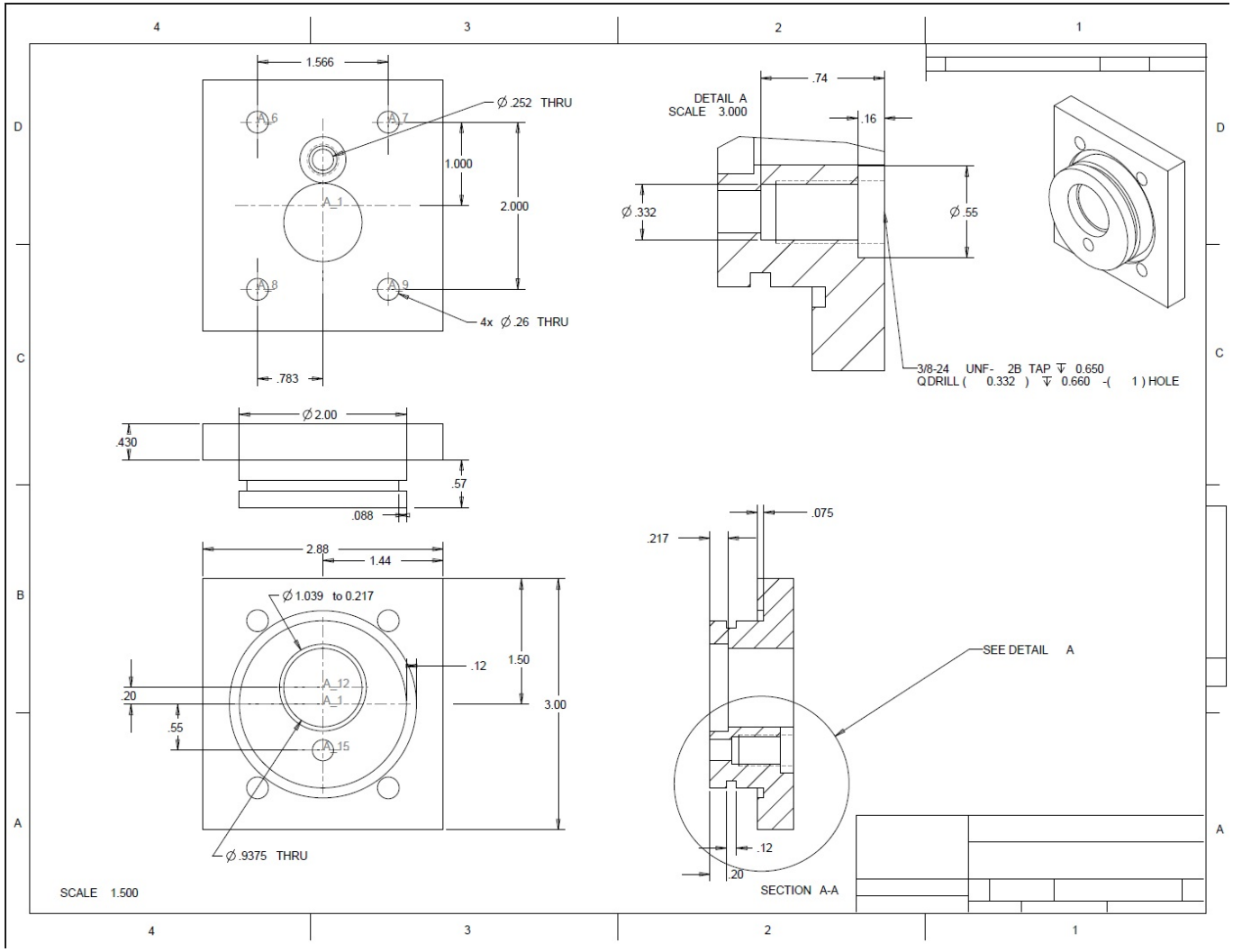

Figure B.1: Endwall Drawing

C. Detailed Drawings of Manifold Pieces

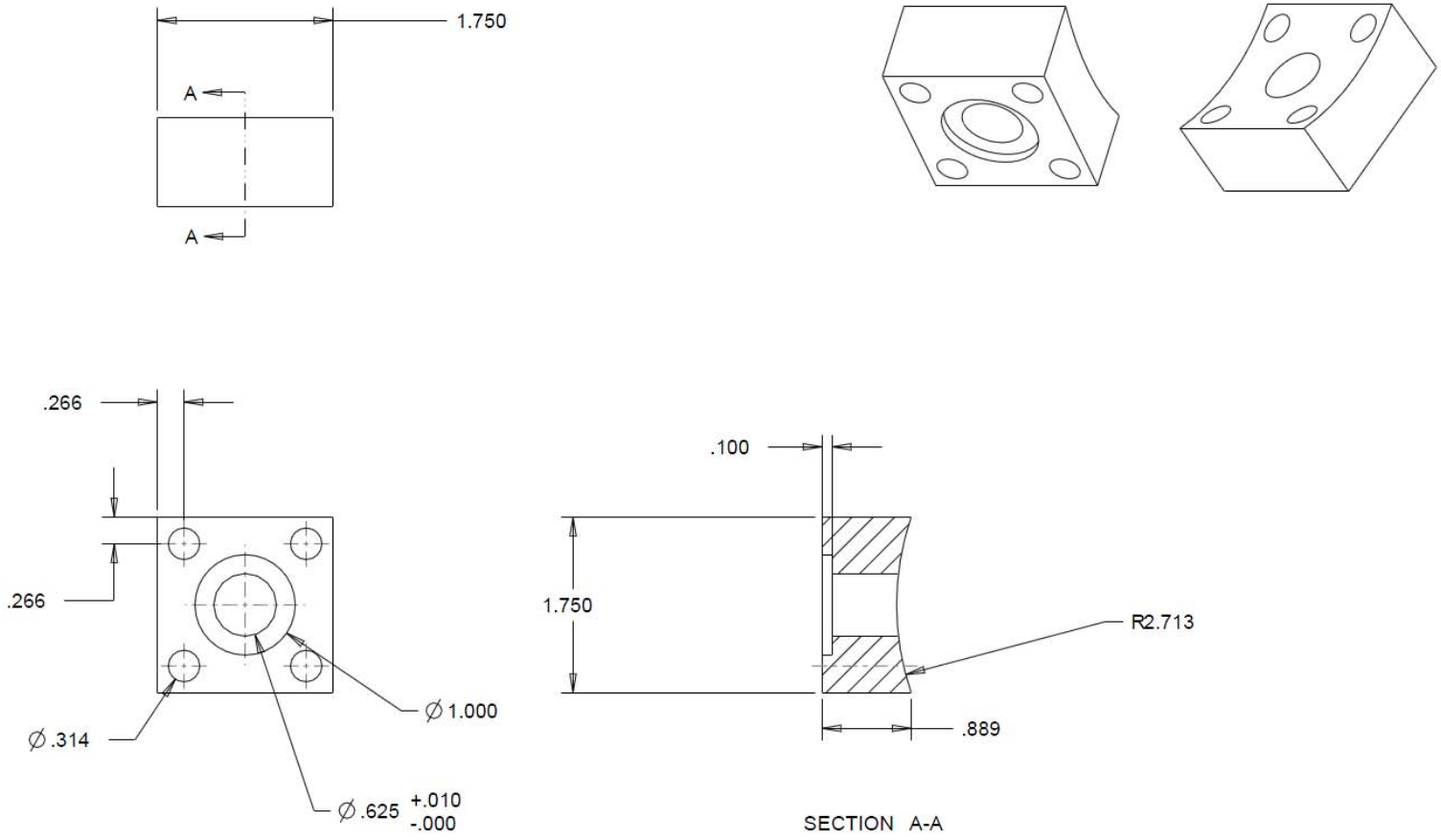

Figure C.1: Manifold Block Piece Drawing

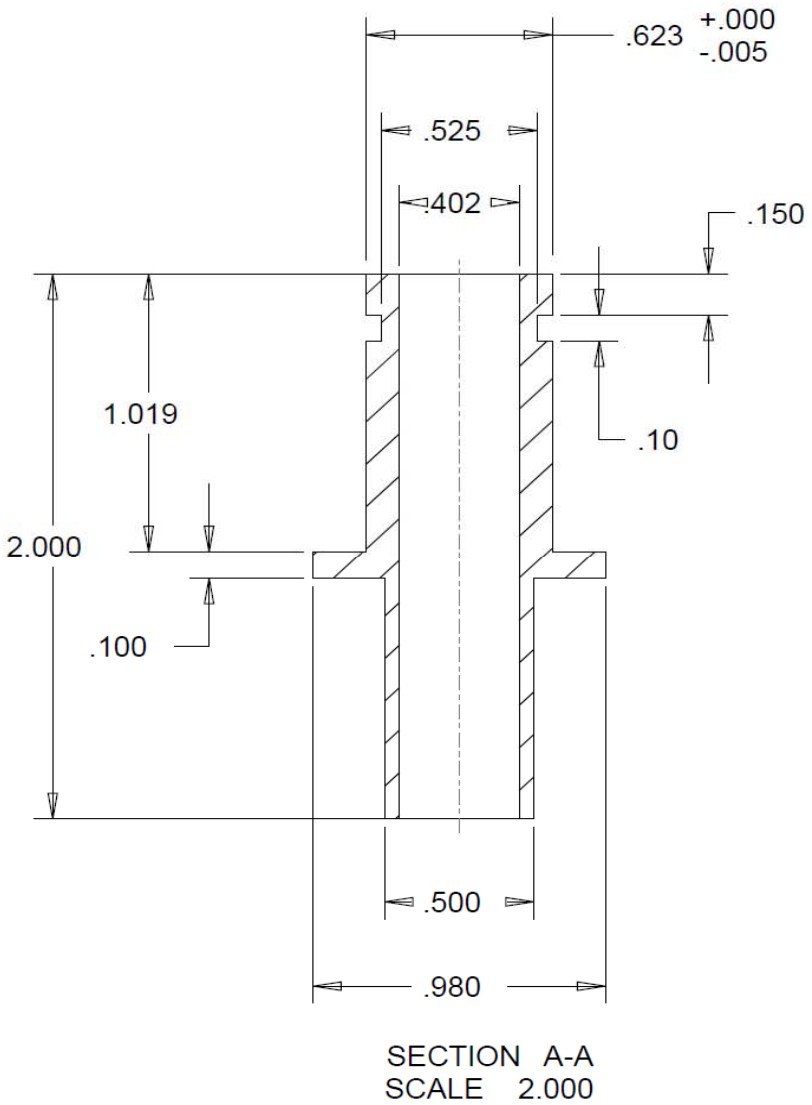

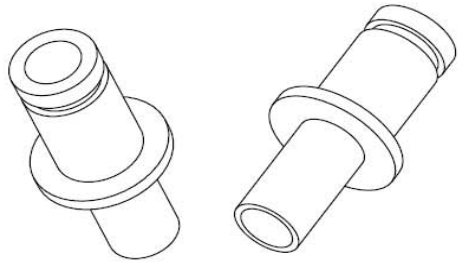

Figure C.2: Manifold Tube Piece Drawing

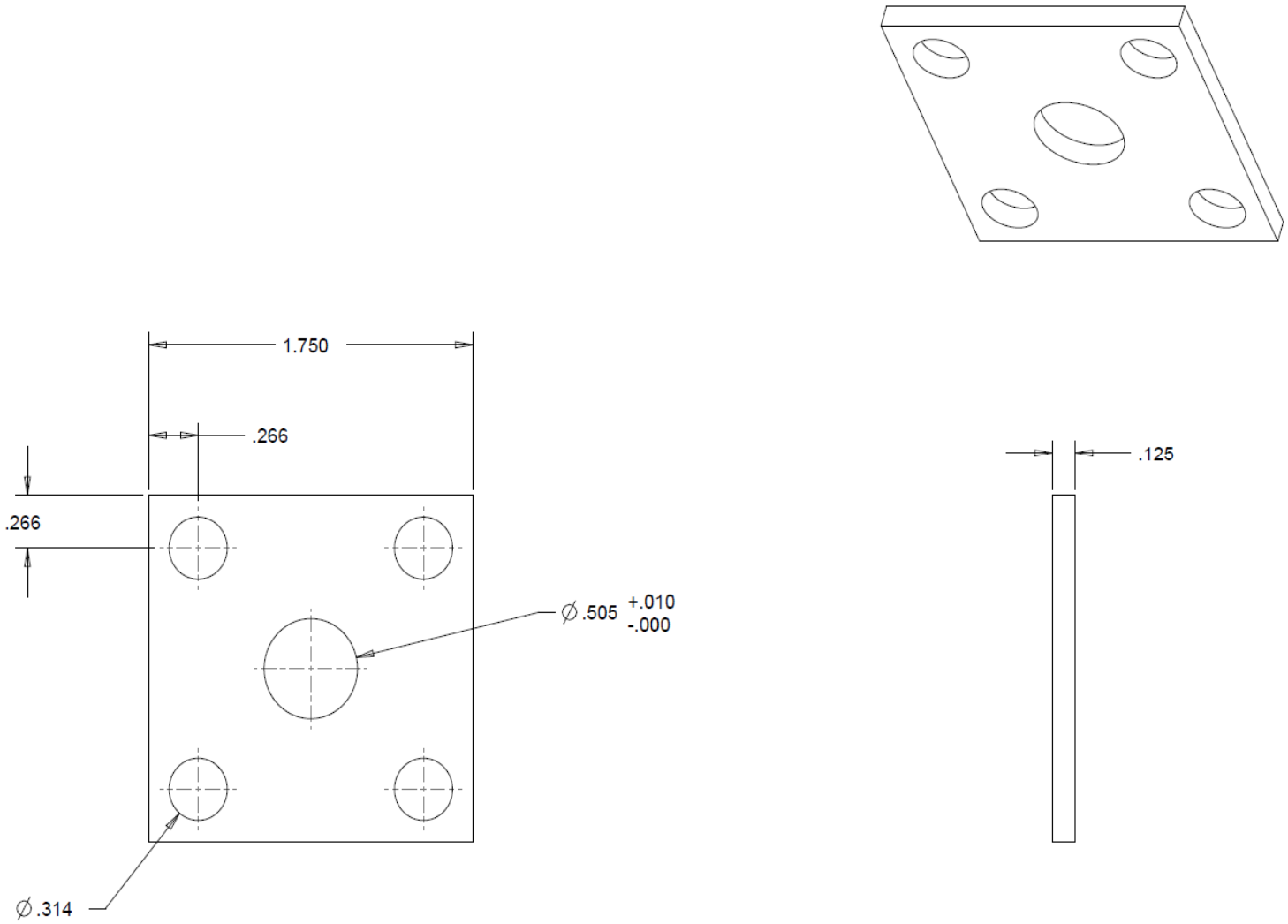

Figure C.3: Manifold Plate Piece Drawing

D. Summary of Peaks in Spectroscopic Outputs

Table D.1 Summary of Peaks

Metal	Peak Location	Cause of Peak
Aluminum	396	Aluminum Doublet
	473	Aluminum Oxide (AlO $B^2\Sigma^+ \rightarrow X^2\Sigma^+$ $\Delta v=0$)
	486	Aluminum Oxide (AlO $B^2\Sigma^+ \rightarrow X^2\Sigma^+$ $\Delta v=-1$)
	515	Aluminum Oxide (AlO $B^2\Sigma^+ \rightarrow X^2\Sigma^+$ $\Delta v=-2$)
	545	Aluminum Oxide (AlO $B^2\Sigma^+ \rightarrow X^2\Sigma^+$ $\Delta v=-3$)
	588	Sodium D-line
	603	Iron Oxide (FeO B→X $\Delta v=3$)
	631	Iron Oxide (FeO B→X $\Delta v=2$)
	644	Iron Emission (NIST)
	657	Iron Oxide (FeO B→X $\Delta v=1$)
	666	Iron Emission (NIST)
	679	Iron Oxide (FeO B→X $\Delta v=0$)
	764	Potassium Doublet
Boron	409	Boron Oxide (BO_2 $B^2\Sigma \rightarrow X^2\Sigma$ transition)
	416	Boron Oxide (BO $A^2\Pi \rightarrow X^2\Sigma$ Transition)
	438	Boron Oxide (BO $A^2\Pi \rightarrow X^2\Pi$ Transition)
	454	Boron Oxide (BO $A^2\Pi \rightarrow X^2\Pi$ Transition)
	475	Boron Oxide (BO $A^2\Pi \rightarrow X^2\Pi$ Transition)
	495	Boron Oxide (BO $A^2\Pi \rightarrow X^2\Pi$ Transition)
	516	Boron Oxide (BO $A^2\Pi \rightarrow X^2\Pi$ Transition)
	547	Boron Oxide (BO $A^2\Pi \rightarrow X^2\Pi$ Transition)
	577	Boron Oxide (BO $A^2\Pi \rightarrow X^2\Pi$ Transition)
	599	Boron Oxide (BO $A^2\Pi \rightarrow X^2\Pi$ Transition)
	619	Boron Oxide (BO $A^2\Pi \rightarrow X^2\Pi$ Transition)
	637	Boron Oxide (BO $A^2\Pi \rightarrow X^2\Pi$ Transition)
Hafnium	515	Hafnium Oxide (B → X transition)
	547	Hafnium Oxide (B → X transition)
	588	Sodium D-line
	764	Potassium Doublet

Table D.1 (cont.)

Metal	Peak Location	Cause of Peak
Magnesium	364	Magnesium Oxide (MgO C→A Δv = 1)
	372	Magnesium Oxide (MgO C→A Δv = 0)
	382	Magnesium Oxide (MgO C→A Δv = -1)
	391	Magnesium Oxide (MgO C→A Δv = -2)
	402	Magnesium Oxide (MgO C→A Δv = -3)
	454	Magnesium Oxide (MgO $B^1\Sigma^+ \rightarrow X^1\Sigma^+$ Δv = 2)
	474	Magnesium Oxide (MgO $B^1\Sigma^+ \rightarrow X^1\Sigma^+$ Δv = 1)
	490	Magnesium Oxide (MgO $B^1\Sigma^+ \rightarrow X^1\Sigma^+$ Δv = -0)
	510	Magnesium Oxide (MgO $B^1\Sigma^+ \rightarrow X^1\Sigma^+$ Δv = -1) (hidden)
	518	Magnesium Triplet or Magnesium Oxide
	552	Magnesium I emission
	588	Sodium D-line
	591	Magnesium Oxide (MgO B→A Δv = 0) (hidden)
	621	Magnesium Oxide (MgO B→A Δv = -1)
	631	Iron Oxide (FeO B→X Δv = 2)
	655	Iron Oxide (FeO B→X Δv = 1)
	666	Iron emission
	679	Iron Oxide (FeO B→X Δv = 0)
	764	Potassium Doublet
Manganese	403	Manganese Emission (403.3 and 403.4 nm)
	520	Manganese Oxide ($A^6\Sigma \rightarrow X^6\Sigma$ Δv=1)
	537	Manganese Oxide ($A^6\Sigma \rightarrow X^6\Sigma$ Δv=0)
	540	Manganese Oxide ($A^6\Sigma \rightarrow X^6\Sigma$ Δv=0)
	559	Manganese Oxide ($A^6\Sigma \rightarrow X^6\Sigma$ Δv=-1)
	588	Sodium D-line
	620	Manganese Oxide ($A^6\Sigma \rightarrow X^6\Sigma$ Δv=-3)
	764	Potassium Doublet
Silicon	<300 nm	Silicon Oxide (SiO)
	331 – 368	Silicon Nitride (SiN_2)
	374 – 500	Silicon Nitride (SiN B → X transition)
	500, 519, 548	Unknown Emission
	588	Sodium D-line
	600 – 700	Iron Impurity (FeO B → X and Fe emission)
	764	Potassium Doublet

Table D.1 (cont.)

Titanium	518	Titanium Oxide (C → X transition)
	545	Titanium Oxide (C → X transition)
	588	Sodium D-line
	764	Potassium Doublet
Zirconium	516	Zirconium Oxide (B → X transition)
	549	Zirconium Oxide (B → X transition)
	588	Sodium D-line
	764	Potassium Doublet
Strontium Chloride	401	Strontium Oxide (SrO B→X transition)
	463	Strontium Emission
	588	Sodium D-line
	603	Strontium Chloride (SrCl $B^2\Sigma^+ \rightarrow X^2\Sigma^+$ $\Delta v=2$)
	619	Strontium Chloride (SrCl $B^2\Sigma^+ \rightarrow X^2\Sigma^+$ $\Delta v=1$)
	631	Strontium Chloride (SrCl $B^2\Sigma^+ \rightarrow X^2\Sigma^+$ $\Delta v=0$)
	643	Strontium Chloride (SrCl $B^2\Sigma^+ \rightarrow X^2\Sigma^+$ $\Delta v=-1$) or Strontium Hydroxide
	658	Strontium Chloride (SrCl $B^2\Sigma^+ \rightarrow X^2\Sigma^+$ $\Delta v=-2$) or Strontium Hydroxide
	665	Strontium Chloride (SrCl $B^2\Sigma^+ \rightarrow X^2\Sigma^+$ $\Delta v=-3$) or Strontium Hydroxide
	678	Strontium Chloride (SrCl $B^2\Sigma^+ \rightarrow X^2\Sigma^+$ $\Delta v=-4$) or Strontium Hydroxide
	702	Strontium Chloride (SrCl $B^2\Sigma^+ \rightarrow X^2\Sigma^+$ $\Delta v=-5$) or Strontium Hydroxide
	722	Strontium Chloride (SrCl $B^2\Sigma^+ \rightarrow X^2\Sigma^+$ $\Delta v=-6$) or Strontium Hydroxide
	764	Potassium Doublet

Table D.1 (cont.)

Scandium	464	Unknown Emission
	476	Scandium Oxide (ScO $B^2\Sigma^+ \rightarrow X^2\Sigma^+$ $\Delta v = 0$)
	496	Scandium Oxide (ScO $B^2\Sigma^+ \rightarrow X^2\Sigma^+$ $\Delta v = -1$)
	517	Scandium Oxide (ScO $B^2\Sigma^+ \rightarrow X^2\Sigma^+$ $\Delta v = -2$)
	560	Scandium Oxide (ScO A → X $\Delta v = 1$)
	588	Scandium Oxide (ScO A → X $\Delta v = 0$) (hidden)
	588	Sodium D-Line
	610	Scandium Oxide (ScO A' → X $\Delta v = 1$)
	622	Scandium Oxide (ScO A → X $\Delta v = -1$)
	644	Scandium Oxide (ScO A' → X $\Delta v = 0$) or Iron Emission
	660	Scandium Oxide (ScO A → X $\Delta v = -2$) or Iron Emission
	676	Scandium Oxide (ScO A' → X $\Delta v = -1$) or Iron Oxide (FeO B→ X $\Delta v = 0$)
	764	Potassium Doublet